HHS Public Access

Author manuscript

Neuron. Author manuscript; available in PMC 2021 July 08.

Published in final edited form as:

Neuron. 2020 July 08; 107(1): 126–143.e8. doi:10.1016/j.neuron.2020.03.033.

TMIE defines pore and gating properties of the mechanotransduction channel of mammalian cochlear hair cells

Christopher L. Cunningham[1,*], **Xufeng Qiu**[1,*], **Zizhen Wu**[1], **Bo Zhao**[2], **Guihong Peng**[1], **Ye-Hyun Kim**[3], **Amanda Lauer**[3], **Ulrich Müller**[1,#]

[1]The Solomon H. Snyder Department of Neuroscience, Johns Hopkins University School of Medicine, Baltimore, MD 21205, USA.

[2]Department of Otolaryngology Head & Neck Surgery, Indiana University School of Medicine Indianapolis, IN 46202, USA.

[3]Department of Otolaryngology-HNS, Johns Hopkins University School of Medicine, Baltimore, MD 21205, USA.

Summary

TMC1 and TMC2 have been proposed to form the pore of the mechanotransduction channel of cochlear hair cells. Here we show that TMC1/2 cannot form mechanotransduction channels in cochlear hair cells without TMIE. TMIE binds to TMC1/2 and a TMIE mutation that perturbs TMC1/2 binding abolishes mechanotransduction. N-terminal TMIE deletions affect the response of the mechanotransduction channel to mechanical force. Similar to mechanically gated TREK channels, the C-terminal cytoplasmic TMIE domain contains charged amino acids that mediate binding to phospholipids including PIP_2. TMIE point mutations in the C-terminus that are linked to deafness disrupt phospholipid binding, sensitize the channel to PIP_2 depletion from hair cells, and alter the channel's unitary conductance and ion selectivity. We conclude that TMIE is a subunit of the cochlear mechanotransduction channel, and that channel function is regulated by a phospholipid-sensing domain in TMIE with similarity to those in other mechanically gated ion channels.

Graphical Abstract

[#]Lead contact: Ulrich Müller, The Solomon H. Snyder Department of Neuroscience, Johns Hopkins University School of Medicine, Baltimore, MD 21205, USA. umuelle3@jhmi.edu, 442-287-4762.

[*]equal author contribution

Author Contributions

CLC carried out genetic, immunohistological, biochemical experiments and generated mutant mice, ZW contributed to electrophysiological recordings, which were mostly carried out by XQ. BZ contributed immunolocalization studies, GP assisted with molecular cloning, Y-HK and AL carried out ABR recordings. CLC, XQ and UM designed the study. All authors contributed to data analysis. CLC, XQ and UM wrote the manuscript.

Declaration of Interests

Dr. Mueller is a co-founder of Decibel Therapeutics.

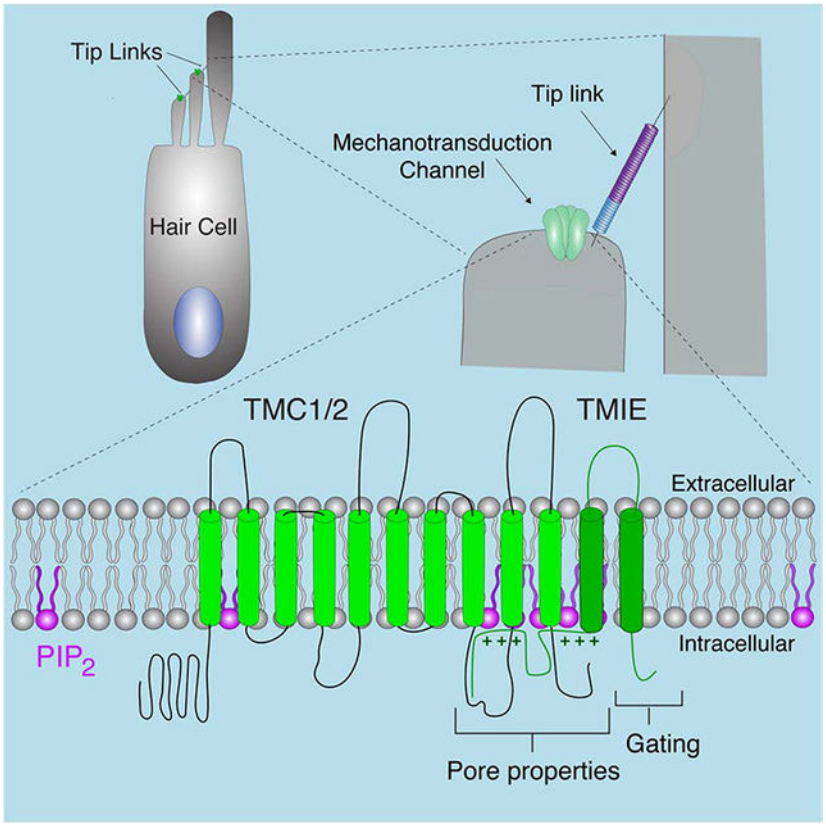

ETOC Paragraph

Cunningham et al. demonstrate that the transmembrane protein TMIE is an essential subunit of the sensory mechanotransduction channel of cochlear hair cells. TMIE mutations linked to deafness affect the pore properties of the mechanotransduction channel. The authors also identify PIP_2 binding domains in TMIE that regulate TMIE function in mechanotransduction.

INTRODUCTION

Mechanotransduction, the conversion of mechanical stimuli into electrochemical signals, is critical for our ability to perceive touch, sense sound and to guide many other physiological processes such as the control of blood pressure. Tremendous progress has been made in the identification of mechanically-gated ion channels in many tissues (Delmas and Coste, 2013; Ranade et al., 2015), yet the molecules that form the mechanotransduction channels critical for sound perception have remained a topic of debate. These ion channels are localized in the stereocilia of cochlear hair cells near the lower end of tip links (Beurg et al., 2009), the extracellular filaments that connect the stereocilia and gate the transduction channels (Fig. 1A) (Assad et al., 1991; Basu et al., 2016; Zhao et al., 1996).

TMC1, TMC2, LHFPL5 and TMIE have been implicated to be components of the mechanotransduction channel of hair cells (Beurg et al., 2015a; Beurg et al., 2014; Beurg et al., 2015b; Kim et al., 2013; Pan et al., 2018; Pan et al., 2013; Xiong et al., 2012; Zhao et al., 2014). These proteins are localized near the lower end of tip links (Fig. 1A) and interact with

the tip-link protein PCDH15 (Beurg et al., 2015b; Ge et al., 2018; Kurima et al., 2015; Maeda et al., 2014; Mahendrasingam et al., 2017; Xiong et al., 2012; Zhao et al., 2014). Mutations in the genes encoding these proteins perturb mechanotransduction and affect hearing (Kawashima et al., 2011; Xiong et al., 2012; Zhao et al., 2014).

TMC1 and TMC2 are expressed in developmentally regulated patterns in cochlear hair cells and have at least in part redundant functions (Kawashima et al., 2011; Kim and Fettiplace, 2013; Kurima et al., 2015). Recent studies suggest that TMC1 and TMC2 are pore-forming subunits of the mechanotransduction channel in hair cells. Consistent with this model, the unitary channel conductance and Ca^{2+} permeability of the mechanotransduction channel differs between hair cells that express only TMC1 or only TMC2 (Corns et al., 2017; Kim and Fettiplace, 2013; Pan et al., 2013). A M412K point mutation in TMC1 affects the Ca^{2+} permeability of the channel (Beurg et al., 2015a; Corns et al., 2016; Pan et al., 2013). Channel conductance is also perturbed by cysteine modification agents in hair cells overexpressing TMC1 proteins carrying engineered cysteine mutations (Pan et al., 2018). Finally, truncated turtle TMC1/2 proteins when reconstituted into artificial lipid bilayers have been reported to form mechanically-activated ion channels (Jia et al 2020). Surprisingly, studies by Liu et al (2019) suggest that TMC1 provides a leak conductance in hair cells that is sensitive to some of the same cysteine mutations affecting mechanotransduction. A similar function as a leak channel has been reported for TMC proteins in worms (Yue et al., 2018). Thus, TMC1 has been proposed to be part of at least two distinct ion channels in hair cells.

The functions of LHFPL5 and TMIE within the mechanotransduction complex of hair cells are unclear. LHFPL5 shares structural and functional homology with TARP proteins, which allosterically regulate pore-properties of glutamate receptors (Xiong et al., 2012). TMIE has no known homology to any mammalian protein. LHFPL5 regulates TMC1 localization to stereocilia in hair cells of mice (Beurg et al., 2015b), and TMIE affects TMC1/2 localization to stereocilia of hair cells in zebrafish (Pacentine and Nicolson, 2019), suggesting that LHFPL5 and TMIE might regulate protein transport. However, LHFPL5 and TMIE are present within the mechanotransduction complex at tip links (Xiong et al., 2012; Zhao et al., 2014), suggesting a more direct role for these proteins in transduction. Defects in TMC1/2 localization in *Lhfpl5* and *Tmie* mutants could be an epiphenomenon caused by incomplete assembly of an ion channel complex.

We now provide evidence that TMIE is a subunit of the sensory mechanotransduction channel in cochlear hair cells. We show that N-terminal TMIE deletions affect the gating properties of the mechanotransduction channel, suggesting that this part of TMIE is important for force transmission onto the channel. C-terminal TMIE mutations affect its binding to TMC1/2 and lead to changes in channel conductance and ion selectivity, indicating that this part of TMIE regulates pore properties of the transducer channel. Intriguingly, the C-terminal cytoplasmic domain of TMIE binds to PIP_2, suggesting that some of the previously reported PIP_2 effects on channel function (Effertz et al., 2017; Hirono et al., 2004) are mediated by TMIE. A similar charged cytoplasmic domain has been observed in the mechanically gated TREK channel (Chemin et al., 2005; Chemin et al.,

2007), suggesting that several mechanically gated ion channels with distinct physiological functions are regulated by a common mechanism.

RESULTS

Generation of TMC1-HA and TMC2-MYC mice

Available antibodies to TMC1 and TMC2 lead in our hands to inconsistent results in immunolocalization studies. To facilitate the analysis of TMC1 and TMC2 distribution in hair cells, we modified the endogenous *Tmc1* and *Tmc2* genomic loci and introduce an HA-tag and a MYC-tag at the C-terminus of TMC1 and TMC2, respectively (Fig. 1B). Versions of TMC1 and TMC2 containing epitope tags have been studied but relied on BAC transgenic mice (Kurima et al., 2015). We modified the endogenous genomic *Tmc1* and *Tmc2* loci to minimize potential undesired effects of random transgene insertions.

Measurements of the auditory brainstem response (ABR) in homozygous $Tmc1^{HA/HA}$ and $Tmc2^{MYC/MYC}$ mice at 4–6 weeks of age revealed normal auditory thresholds (Fig. S1A,D). The mice did not show head-bobbing or circling, indicating that vestibular function was preserved (data not shown). We next measured mechanotransduction currents in the mid-apical region of the cochlear duct. TMC2 expression increases in cochlear hair cells between P0 and P3 and is downregulated by P5–7. TMC1 expression is low until P3 but thereafter is upregulated (Kawashima et al., 2011; Kim and Fettiplace, 2013; Kurima et al., 2015). Recordings for TMC1-HA mice were therefore carried out at P6–7 and for TMC2-MYC at P3. Hair bundles of OHCs were stimulated with a stiff glass probe by stepwise deflections ranging from −400 to 1000 nm. Mechanotransduction (MET) currents were recorded by patching onto the cell body of hair cells. MET currents were indistinguishable between wild-type, $Tmc1^{HA/HA}$ and $Tmc2^{MYC/MYC}$ mice (Fig. S1B,C,E,F). Current/displacement plots revealed no noticeable difference in the kinetics of transducer currents or in their peak amplitudes at maximal hair bundle deflections (Fig. S1C,F). We conclude that the HA-tags do not significantly interfere with TMC1/2 function.

Effects of TMIE on the localization of TMC1-HA and TMC2-MYC

Using antibodies against HA and MYC, we analyzed in cochlear whole mounts the distribution of TMC1-HA and TMC2-MYC in hair cells in the mid-apical region of the cochlea. Stereocilia were visualized by staining their F-actin cytoskeleton with phalloidin. Consistent with earlier reports (Kawashima et al., 2011; Kim and Fettiplace, 2013; Kurima et al., 2015), we observed TMC1-HA expression in stereocilia of OHCs and IHCs at P7 (Fig. 1C) but not at P3 (Fig. S4F). TMC1-HA was more difficult to detect in IHCs compared to OHCs because of low expression levels in IHCs, requiring longer exposure times for imaging (Fig. 1C). Surprisingly, in optical sections from the apex to the base of hair cells, TMC1-HA was found in high abundance in the cell body (Fig. 1C). TMC-1 localization to the cell body, and differences in expression levels between OHCs and IHCs, were confirmed in histological sections (Fig. 1E). In contrast to TMC1, TMC2 was expressed prominently at P3 (Fig. 1D) as reported (Kawashima et al., 2011; Kim and Fettiplace, 2013; Kurima et al., 2015), and it was present at similar levels in the stereocilia of IHCs and OHCs, with no detectable protein in the cell body (Fig. 1D). It was surprising that TMC1 is prominently

expressed in the cell bodies of hair cells, which is unlike the distribution of other components of the mechanotransduction complex.

Previous studies suggested that TMIE does not affect TMC1/2 distribution in murine hair cells, an interpretation that was based on the analysis of the localization of TMC1/2 following their overexpression in hair cells from *Tmie*$^{-/-}$ mice (Zhao et al., 2014). In contrast, studies in zebrafish indicate that TMIE affects the distribution of TMC1 and TMC2b in this vertebrate species (Pacentine and Nicolson, 2019). To analyze effects of TMIE on TMC1 distribution in murine hair cells when expressed at or near endogenous levels, we generated by crossings *Tmie*$^{-/-}$*Tmc1*$^{HA/HA}$ and *Tmie*$^{-/-}$*Tmc2*$^{MYC/MYC}$ mice. We stained cochlear whole mounts of *Tmie*$^{-/-}$*Tmc1*$^{HA/HA}$ mice at P7 with antibodies to HA, and of *Tmie*$^{-/-}$*Tmc2*$^{MYC/MYC}$ mice at P3 with antibodies to MYC. TMC1-HA was no longer detected in the stereocilia of hair cells in *Tmie*$^{-/-}$*Tmc1*$^{HA/HA}$ mice but was still present in the cell body (Fig. 1C), indicating that TMIE is necessary to maintain TMC1 stereocilia localization but not expression (Fig. 1C). TMC2-MYC was localized to the stereocilia of hair cells in *Tmie*$^{-/-}$*Tmc2*$^{MYC/MYC}$ mice, but at reduced levels, and some protein was present in the cell body (Fig. 1D).

We next analyzed the distribution of PCDH15, CDH23, LHFPL5 and PMCA2 in *Tmie*$^{-/-}$ hair cells at P2–P7 using antibodies against endogenously expressed protein. There were no obvious defect in the localization of these proteins in *Tmie*$^{-/-}$ hair cells (Fig. S1G–J).

Neither TMC1 nor TMC2 affect TMIE localization

To determine whether TMC1 or TMC2 affect the localization of TMIE to stereocilia, we introduce an HA-epitope tag at the C-terminus of the endogenous *Tmie* gene to facilitate detection of TMIE (Fig. 2A). Homozygous *Tmie*$^{HA/HA}$ mice showed normal ABR responses (Fig. 2B), mechanotransduction (Fig. 2C,D) and vestibular function (data not shown). Consistent with earlier findings (Zhao et al., 2014), TMIE-HA was present in the stereocilia of IHCs and OHCs (Fig. 2D), with additional staining in the cell body (Fig. 2E). Similar observations were made with a second genetically modified mouse line where we introduced three MYC-tags at the C-terminus of TMIE (Fig. 2F). TMIE-HA localization to stereocilia appeared unaffected in hair cells from mutant mice lacking both TMC1 and TMC2 (Fig. 2G, H).

TMIE is essential for TMC1 and TMC2 function in mechanotransduction

To test whether TMC1 and TMC2 can form mechanotransduction channels in hair cells without TMIE, we took advantage of our injectoporation procedure that allows us to overexpress proteins in hair cells in cochlear explants (Fig. 3A) (Xiong et al., 2014). We generated expression vectors containing cDNAs for TMC1 and TMC2 modified to encode epitope tags at their N- or C-termini (MYC-TMC1, TMC1-HA, MYC-TMC2, TMC2-MYC) (Fig. 3B). To verify that the epitope-tagged proteins were functional, we expressed them by injectoporation at P3 in hair cells from mutant mice lacking both TMC1 and TMC2 and asked whether they could reconstitute mechanotransduction channels in the mutant hair cells. Mechanotransduction currents were recorded one day after injectoporation by stimulating hair bundles of OHCs with a stiff glass probe. Because of variability in bundle

shape following injectoporation, a probe with approximate bundle size was lowered onto the bundle from the top. Hair bundles were stimulated with deflections ranging from −400 to 1000 nm (Fig. 3C).

Expression of all epitope-tagged TMC1 and TMC2 constructs rescued the mechanotransduction defects in OHCs from *Tmc1/2* double mutants (Fig. 3C,D). Expression of MYC-TMC2 and TMC2-MYC led to larger peak amplitudes at saturating mechanical stimuli than expression of MYC-TMC1 and TMC1-HA (300 ± 57 pA for MYC-TMC2; 322 ± 58 pA for TMC2MYC; 183 ± 35 pA for TMC1-HA; 181 ± 39 pA for MYC-TMC1) (Fig. 3C,D). This finding is consistent with earlier reports (Kawashima et al., 2011; Pan et al., 2013). It is currently unclear why TMC2 leads to more efficient rescue of transduction than TMC1. There was no difference in the extent of rescue between MYC-TMC2 and TMC2-MYC, or between MYC-TMC1 and TMC1-HA (Fig. 3C,D). We therefore used TMC1/2 constructs with epitope tags at the N- or C-terminus interchangeably.

Next, we expressed by injectoporation TMC1-HA, MYC-TMC2 and control TMIE-HA (Fig. 3A,B) in OHCs from *Tmie*$^{-/-}$ mice at P3. Protein distribution and mechanotransduction were evaluated one day later. We chose these time points because our earlier studies have shown that at this age, the morphology of *Tmie*$^{-/-}$ hair bundles is not significantly altered and tip links are maintained (Zhao et al., 2014). The TMC1-HA, MYC-TMC2 and TMIE-HA proteins localized to stereocilia of *Tmie*$^{-/-}$ hair cells (Fig. 3E). Using Imaris 9.1 software, we generate 3D reconstructions of stained hair bundles. These studies confirmed that endogenous TMC1/2 proteins are broadly expressed along the length of stereocilia (Fig. S2A,B). Epitope tagged TMC1/2 expressed by injectoporation showed a similar broad distribution (Fig. S2C,D). However, unlike control TMIE-HA, neither TMC1-HA nor TMC2-MYC rescued the mechanotransduction defects in OHCs from *Tmie*$^{-/-}$ mice (Fig. 3E,F). Similar observations were made in IHCs (Fig. S2E,F). We conclude that TMC1 and TMC2 cannot form functional mechanotransduction channels in OHCs and IHCs without TMIE.

TMC1 and TMC2 are essential for TMIE function

Next we tested whether TMIE can form mechanotransduction channels in hair cells without TMC1 and TMC2. For these experiments, we used our TMIE-HA expression construct (Fig. 3B) that rescues mechanotransduction in hair cells from *Tmie*$^{-/-}$ mice (Fig. 3E,F). We injectoporated TMIE-HA into P3 OHCs from *Tmc1/2* double mutants. One day later, TMIE-HA was localized to stereocilia of mutant hair cells (Fig. 3G), but mechanotransduction currents could not be evoked (Fig. 3G,H). TMIE thus cannot form a mechanotransduction channel in OHCs in the absence of TMC1 and TMC2.

TMIE binds to TMC1 and TMC2

TMIE might interact with TMC1/2 to form an ion channel, but our previous attempts to demonstrate interaction between TMIE and TMC1/2 by co-immunoprecipitation (co-IP) following their heterologous expression in HEK cells had failed (Zhao et al., 2014). Our initial CMV expression vectors for TMC1 and TMC2 gave low expression levels, and protein-protein interactions were evaluated in a HEPES buffer containing 140 mM NaCl and

1% Triton X-100 (Zhao et al., 2014). Expression levels were significantly improved by using a CAG promoter, and robust co-IP was observed between TMIE-HA and MYC-TMC1 in a Tris buffer containing 150mM NaCl, 1% NP40 and 0.1% SDS (Fig. 4B). Conversely, TMIE-HA could be co-IPed with TMC1-FLAG and TMC2-FLAG under these buffer conditions (Fig. 4C,D). No co-IP was observed between TMIE-HA and MYC-ARF6, an unrelated control protein with functions in the trafficking of membranes and proteins (D'Souza-Schorey et al., 1998; Zaoui et al., 2019) (Fig. 4B). We conclude that TMC1 and TMC2 can bind to TMIE.

The N-terminal part of TMIE is dispensable for TMC1 binding but affects channel gating

We hypothesized that mutations that affect interactions between TMIE and TMC1 would prevent the formation of a functional ion channel. We therefore thought to identify mutations in TMIE that disrupt TMC1 binding. We initially generated TMIE-HA constructs lacking the predicted N-terminal cytoplasmic domain (TMIE-11–153-HA) or lacking a longer N-terminal portion including the first TM domain (TMIE-28–153-HA) (Fig. 4E). Using extracts from HEK cells that had been transfected to express MYC-TMC1 with TMIE-HA, TMIE-11–153-HA or TMIE-28–153-HA (Fig. 4E), we observed in co-IPs quantitatively similar interactions of all three TMIE proteins with MYC-TMC1 (Fig. 4F, G) and MYC-TMC2 (data not shown). These findings suggest that the C-terminal portion of TMIE contains a TMC1 binding site, although they do not exclude that the N-terminus contributes to binding.

Although the TMIE constructs with N-terminal deletions did not affect interactions of TMIE with TMC1/2, we wondered whether they would affect TMIE function. We expressed TMIE-HA, TMIE-11–153-HA and TMIE-28–153-HA by injectoporation in hair cells from wild-type animals and *Tmie*$^{-/-}$ mutants and analyzed TMIE distribution and mechanotransduction. All three proteins localized to stereocilia of OHCs (Fig. 4H), with no quantitative differences (Fig. 4I). TMIE-11–153-HA but not TMIE-28–153-HA rescued mechanotransduction as efficiently as full-length TMIE-HA (Fig. 4J,K). The amplitudes of saturated mechanotransduction currents at maximal hair bundle deflection following expression of TMIE-HA and TMIE-11–153-HA were at 331 ± 40 pA and 384 ± 34 pA, respectively, but for TMIE-28–153-HA was at 91 ± 14 pA, suggesting that the number of transducer channels or their activity was affected by the N-terminal deletion in TMIE-28–153-HA (Fig 4K). Plots of the open probability of the transduction channel (P_o) against displacement revealed that the curve obtained from hair cells expressing TMIE-28–153-HA was shifted to the right and broadened when compared to hair cells expressing TMIE-HA or TMIE-11–153-HA (Fig. 4L), indicate that the response of the mechanotransduction channel to force and/or the kinetics of channel gating was altered by the TMIE-28–153 mutation. Thus, even though the N-terminal TMIE part is not essential for binding to TMC1/2, it is critical for normal function of TMIE in mechanotransduction.

The C-terminal cytoplasmic domain of TMIE is critical for TMC1 binding and mechanotransduction

To identify TMIE domains critical for binding to TMC1/2, we generated additional cDNA constructs. In TMIE-CDTM-HA, we swapped the transmembrane domains of TMIE with

the transmembrane domains of CD6 and CD7 (Fig. 5A). CD6 and CD7 are critical for immune cell function but are not linked to ion channel function (Lee et al., 1998; Orta-Mascaro et al., 2016). We also generated three constructs with deletions in the C-terminal cytoplasmic domain of TMC1 (TMIEdel80–100-HA, TMIEdel101–121-HA, TMIEdel122–142-HA) (Fig. 5A). In co-IP experiments, there was no quantitative difference in the interaction of MYC-TMC1 with TMIE-HA, TMIE-CDTM-HA and TMIEdel122–142 (Fig. 5B–D). However, interactions of MYC-TMC1 with TMIEdel80–100-HA and TMIEdel101–121-HA were impaired (Fig. 5B,D).

For functional tests, we focused on TMIEdel80–100-HA, which reduced interactions with MYC-TMC1 by nearly 80%. TMIEdel80–100-HA efficiently localized to the hair bundles of OHCs that had been injectoporated to express the mutant protein (Fig. 5E,F). While control TMIE-HA rescued mechanotransduction defects in $Tmie^{-/-}$ hair cells, TMIEdel80–100-HA did not rescue the defects (Fig. 5G,H). These data suggest that complex formation between TMIE and TMC1 is critical for the formation of functional mechanotransduction channels in OHCs.

Effects of TMIE point mutations on TMC1/2 binding and localization

Three point mutations in the TMIE C-terminal cytoplasmic tail near the second transmembrane domain are linked to deafness (Fig. 6A) (Naz et al., 2002). These point mutations (R82C, R85W, R93W) reside in the protein domain of TMIE that is critical for its interaction with TMC1/2 (Fig. 5B,D). Surprisingly, none of the mutations noticeably affected interactions between TMIE and TMC1 (Fig. 6B,E) or TMC2 (data not shown).

To further investigate the mechanisms by which the point mutations linked to deafness affect TMIE function we generated genetically modified mouse lines carrying TMIE point mutations. We have shown that the R93W mutation, but not the R82C and R85W mutations, affects TMIE localization to stereocilia (Fig. 6C,D) (Zhao et al., 2014). We thus only generated $Tmie^{R82C/R82C}$ and $Tmie^{R85W/R85W}$ mouse lines, both of which showed similar phenotypes. Unlike mice heterozygous for the point mutations, the homozygous $Tmie^{R82C/R82C}$ and $Tmie^{R85W/R85W}$ mice were deaf (Fig. S3B,D). Similar to $Tmie^{-/-}$ mutants (Zhao et al., 2014), the morphology of stereociliary bundles of hair cells at P5 was only mildly altered in $Tmie^{R82C/R82C}$ and $Tmie^{R85W/R85W}$ mice (Fig. S3A,C). We thus focused our electrophysiological experiments on hair cells during the time period (P0–P7) when stereocilia morphology was largely normal.

We reasoned that while the $Tmie^{R82C}$ and $Tmie^{R85W}$ mutations did not abolish interactions between TMIE and TMC1/2 proteins, they might affect the function of the TMIE-TMC1/2 protein complex in subtle ways. To test this hypothesis, we first analyzed effects of the $Tmie^{R82C}$ and $Tmie^{R85W}$ mutations and TMC1/2 distribution in hair cells. We generated by crossings four mouse lines: $Tmie^{R82C/R82C};Tmc1^{HA/HA}$, $Tmie^{R82C/R82C};Tmc2^{MYC/MYC}$, $Tmie^{R85W/R85W};Tmc1^{HA/HA}$ and $Tmie^{R85W/R85W};Tmc2^{MYC/MYC}$. We then evaluated in the mid-apical cochlear region TMC1 localization at P5–6, and TMC2 localization at P3–4, at peak times of TMC1 and TMC2 expression, respectively (Kawashima et al., 2011; Kurima et al., 2015). The $Tmie^{R82C/R82C}$ and $Tmie^{R85W/R85W}$ mutations affected the localization of TMC1, and to a lesser extent of TMC2, to hair bundles (Fig. 6F,G; Fig. S3E,F).

Effects of TMIE point mutations on mechanotransduction

We next analyzed mechanotransduction in P5 OHCs from *Tmie*$^{R82C/R82C}$ and *Tmie*$^{R85W/R85W}$ mutant mice. As expected from the reduced expression of TMC1 and TMC2 in the hair bundles of the mutants (Fig. 6F,G; Fig. S3E,F), mechanotransduction currents were drastically reduced (Fig. 7A,B; Fig. S4A,B). Plots of the open probability of the transducer channel (P_o) against displacement (Fig. 7C; Fig S4C), revealed no additional defects in the sensitivity of the transducer currents in the mutants. Similar observations were made in IHCs from *Tmie*$^{R82C/R82C}$ mice (Fig. S4D,E).

To analyze if TMIE mutations might affect channel function directly, we analyzed single channel currents focusing on hair cells at P3. We chose this age because significant amounts of TMC2 remain in the hair bundles from *Tmie*$^{R82C/R82C}$ and *Tmie*$^{R85W/R85W}$ mice at P3 (Fig. 6G; Fig. S3F). In addition, even in wild-type mice, TMC2 but not TMC1 is prominently localized to P3 hair bundles (Fig. 1, Fig. S4F) thus allowing us to study effects of TMIE mutations specifically in the context of one of the two TMC proteins. To confirm that mechanotransduction curents in the mid-apical cochlea at P3 solely were dependent on TMC2 as reported (Beurg et al., 2018), we analyzed mechanotransduction in mutant mice that lacked TMC1 but still expressed TMC2 and vice versa. Mechanotransduction currents were nearly indistinguishable between P3 wild-type OHCs from the mid-apical region compared to P3 OHCs from mutant mice that lacked TMC1 but still expressed TMC2, while loss of TMC2 but not TMC1 led to almost complete lack of mechanotransduction currents at P3 (Fig. S4G).

To analyze single channel currents, tip links were disrupted by delivering 5 mM EGTA solution with a fluid jet to hair cells at 40% of the distance along the cochlea from the low frequency end. Following a brief recovery period, mechanotransduction channels were activated with a piezo stimulator and channel activity was recorded in the whole-cell configuration. Fig. 7D and Fig. S5A show typical single channel events that were obtained with a 300 nm deflection. Single channel currents were significantly lower in OHCs from *Tmie*$^{R82C/R82C}$ mice compared to controls (Fig. 7E,G; 4.32 ± 0.12 pA in control; 3.40 ± 0.13 pA in *Tmie*$^{R82C/R82C}$). Channel open time was slightly reduced by the mutation (Fig. 7F). Single channel currents were also reduced in OHCs from *Tmie*$^{R85W/R85W}$ mice (Fig. S5A–C), and in hair cells from mice expressing *Tmie*$^{R85W/R85W}$ but carrying a mutation inactivating TMC1 (Fig. S5D–F), demonstrating that the recorded current depended on TMC2 and not on TMC1.

We next analyzed effects of the TMIE R82C mutations on the Ca^{2+} permeability of the mechanotransduction channel of OHCs by determining the channels reversal potential. Hair cells were recorded with Ca^{2+} and Cs^{+} as the only permeant cations in external and internal solutions respectively (Kim and Fettiplace, 2013, Pan et al., 2013, Kim et al., 2013). We measured the peak amplitude of mechanotransduction currents obtained in varied holding potentials from −89 mV to +111 mV with 20mV stepwise (Fig. 7H) and calculated the reversal potential from current/voltage curves. Fig. 7I shows both current-voltage relations and normalized current-voltage relations to account for differences in absolute values between controls and mutants. Experiments were carried out in *Tmie*$^{R82C/R82C}$ mice carrying a homozygous mutation in TMC1 to ensure that measured values were dependent

on TMC2 but not on TMC1. We observed a slight reduction in the reversal potential (Fig. 7J; 29.37±1.48 mV in *Tmc1*$^{dn/dn}$; *Tmie*$^{R82C/+}$, 23.71 ± 2.03 mV in *Tmc1*$^{dn/dn}$; *Tmie*$^{R82C/R82C}$) and relative Ca^{2+} permeability (Fig. 7K, 6.71 ± 0.70 in *Tmc1*$^{dn/dn}$; *Tmie*$^{R82C/+}$, 4.69 ± 0.63 in *Tmc1*$^{dn/dn}$; *Tmie*$^{R82C/R82C}$) in *Tmie*$^{R82C/R82C}$ mice.

TMIE binds PIP_2 and point mutations linked to deafness affect PIP_2 binding

We were struck by the observation that the R82C and R85W mutations affected mechanotransduction without obvious defects in binding of TMIE to TMC1/2, even though the point mutations are within a domain of TMIE critical for TMC1/2 binding (Fig. 5B,D). Notably, both mutations affect charged amino acids. On closer inspection, we noticed that the C-terminal cytoplasmic domain of TMIE is enriched in positively-charged arginine and lysine residues (20 out of 73 amino acids), including a cluster of six lysine residues between amino acids 124–129 (Fig. 8A). In ion channels, arginine and lysine residues frequently mediate interactions with phospholipids such as PIP_2. We therefore hypothesized that TMIE might bind to phospholipids and that mutations linked to deafness might affect these interactions.

To analyze interactions of TMIE with lipids, we measured the extent to which full-length TMIE and peptides spanning the C-terminal TMIE cytoplasmic domain (Fig. 8A) bind to lipids immobilized on nitrocellulose (Fig. 8B; Fig. S6A). A control binding protein, the phospholipase C-δ1 PH domain, interacted with its known ligands PtdIns(4)P, PIP_2 and PtdIns(3,4,5)P3 but not with other phospholipids (Fig. S6B). Full-length TMIE bound to Phosphatidic Acid (PA), Phosphatidylserine (PS), PtdIns(4)P, PIP_2, and PtdIns(3,4,5)P_3 (Fig. 8B–D; Fig. S6B,C). Peptides encompassing the membrane proximal C-terminal domain of TMIE (amino acid 80–100; TMIE80–100) revealed a similar phospholipid binding profile and additional interactions with cardiolipin (Fig. 8C; S6B,C). A peptide containing amino acids 122–142 of TMIE (TMIE122–142), including the cluster of six lysine residues, bound to multiple phospholipids, while peptides spanning other parts of the C-terminal TMIE domain showed weak or no binding (Fig. 8C; S6B,C). Quantitative analysis of PIP_2 binding revealed strongest interactions with full-length TMIE, and significant binding to TMIE80–100 and TMIE122–142 (Fig. 8D).

TMIE80–100 contains the positively charged amino acid arginine at amino acids 82, 85, and 93, each of which are mutated in genetic forms of hearing loss (Fig. 6A, Fig.8A) (Naz et al., 2002). Single point mutations in these amino acids in TMIE80–100 abolished interactions with PIP_2, while triple mutations were necessary to abolish interactions with PA as well (Fig. 8J, Fig S6D).

We confirmed these results with a second lipid strip containing different combinations of lipids (Fig S6E–H).

We conclude that two regions of the C-terminal cytoplasmic domain of TMIE contribute to phospholipid binding. One of these domains (amino acids 80–100) overlaps with the TMIE protein domain important for TMC1/2 binding, raising the possibility that it mediates coupling between TMC1/2, TMIE and the plasma membrane.

TMIE mutations that affect phospholipid binding affect TMIE function

We next determined whether mutations in the C-terminal domain of TMIE that affect phospholipid binding affect TMIE function. We mutagenized the C-terminal domain of TMIE and asked whether the mutant constructs could rescue mechanotransduction defects in hair cells from *Tmie*$^{-/-}$ mice. Unfortunately, a TMIE deletion construct lacking the entire C-terminal cytoplasmic domain of TMIE could not expressed well enough for experiments (data not shown). However, a TMIE construct lacking amino acids 122–142 (TMIEdel122–142), thus deleting the cluster of six positively charged lysine residues, trafficked into stereocilia as efficiently as full-length TMIE (Fig. 8E,F). Notably, this TMIE domain mediates binding to phospholipids but is not required for TMC1/2 binding (Figs 5C–D, 8C). When injectoporated into P3 OHCs of *Tmie*$^{-/-}$ mice, TMIEdel122–142 rescued mechanotransduction currents less efficiently than full-length TMIE (Fig. 8G,H). At maximal hair bundle deflection, peak currents in OHCs expressing TMIEdel122–142 were reduced (361 ± 19 pA) compared to OHCs expressing full-length TMIE (484 ± 33 pA) (Fig. 8G,H). To normalize for variations in current amplitude, we plotted the open probability of the transducer channel (P_o) against displacement (Fig. 8I). There was no measurable difference in P_o at rest or in the sensitivity of the channel to deflection. When we generated a synthetic TMIE 122–142 peptide and mutated the six lysine residues to alanine, lipid binding was abolished (Fig S6D,H), confirming that those residues are essential for lipid binding.

PIP_2 depletion from hair cells affects TMIE function

PIP_2 binds to TMIE (Fig 8C,D) and depletion of PIP_2 from hair cells affects mechanotransduction by cochlear hair cells (Effertz et al., 2017; Hirono et al., 2004). We therefore wanted to test if we could exploit *Tmie*$^{R82C/R82C}$ mice to provide initial evidence for a functional link between TMIE and PIP_2. While the C-terminal cytoplasmic domain of TMIE contains two major PIP_2 binding regions (amino acid 80–100 and 122–142), we reasoned that mutations affecting one of the regions (such as R82C) might already weaken interactions of TMIE with PIP_2 in the plasma membrane. Consistent with this model, the R82C mutation in TMIE80–100 abolished binding of this protein fragment to PIP_2 (Fig 8J). We therefore compared the effects of PAO treatment, which depletes PIP_2 from hair bundles (Effertz et al., 2017; Hirono et al., 2004), on mechanotransduction currents in P3 OHCs from control and *Tmie*$^{R82C/R82C}$ mice.

Previous studies have evaluated PAO effects on vestibular hair cells and rat IHCs (Effertz et al., 2017; Hirono et al., 2004). In rat IHCs, PAO treatment affects baseline current, reduces peak amplitude of the mechanotransduction currents, affects adaptation and shifts the I/X curve to the right (Effertz et al., 2017). These parameters were similarly altered in wild-type mouse OHCs upon PAO treatment (Fig. 8K,L; Fig. S7A–E). PAO treatment also affected baseline current, peak amplitude and adaptation of the transducer current in OHCs from *Tmie*$^{R82C/R82C}$ mice (Fig. 8K,L; Fig. S7F,G). We did not establish an I/X curve for mutants because currents were very small (Fig. 8K).

In rat IHCs, effects of PAO treatment become more prominent with increasing time of treatment (Effertz et al., 2017). We made similar observations in control mouse OHCs (Fig.

8L). Next, we compared OHCs from *Tmie*$^{R82C/+}$ controls and *Tmie*$^{R82C/R82C}$ mutants. To account for differences in peak transduction currents in mutants compared to controls in the absence of PAO, we normalized the response to peak mechanotransduction currents prior to PAO treatment. Hair cells from *Tmie*$^{R82C/R82C}$ mice were far more sensitive to PIP_2 depletion when compared to controls, an effect that became increasingly evident with increasing time of PAO treatment (Fig. 8L).

In conclusion, the TMIE R82C mutation sensitizes mechanotransduction to PIP_2 depletion, suggesting that the PIP_2 binding site in TMIE is functionally important for mechanotransduction. Since the R82C mutation affects only one of the two PIP_2 binding domains in TMIE, the mutation likely weakens but does not abolish binding of full-length TMIE to PIP_2. Notably, the R82C mutation is immediately next to the plasma membrane within a protein domain that is essential for TMC1/2 binding, suggesting that some of the effects of the mutation on transduction might be caused by perturbation in the interaction between TMIE, PIP_2 and TMC1/2.

DISCUSSION

We provide several lines of evidence that both TMIE and TMC1/2 are subunits of the mechanotransduction channel of cochlear hair cells:(i) TMIE and TMC1/2 are localized to stereocilia of hair cells and bind to each other, and they also interact with the tip-link protein PCDH15 (Zhao et al., 2014); (ii) TMIE is essential for TMC1/2 function in mechanotransduction and vice versa; (iii) a deletion mutation in TMIE that prevents binding to TMC1/2 abolishes mechanotransduction; (iv) a mutation in the N-terminal part of TMIE affects channel gating, indicating that this domain of TMIE is critical to regulate the response of the mechanotransduction channel to force; (v) the C-terminal cytoplasmic TMIE domain contains charged amino acids that mediate binding to phospholipids including PIP_2. TMIE point mutations in the C-terminus that are linked to deafness disrupt phospholipid binding, sensitize the channel to PIP_2 depletion from hair cells, and alter the channel's unitary conductance and ion selectivity. These findings suggest that the mechanotransduction channel in cochlear hair cells is a heteromeric protein complex and that PIP_2 can directly bind to at least one channel subunit.

Previous studies have provided evidence that TMC1 and TMC2 are components of the mechanotransduction channel of cochlear hair cells (see introduction). Most recently, a structural model for TMC1 has been developed based on the known structure of TMEM16A, which has low levels of sequence similarity with TMC1. This homology model predicts a large pore in TMC1 (Ballesteros et al., 2018; Pan et al., 2018). Cysteine mutagenesis experiments indicate that the predicted pore is part of the ion conductance pathway of the mechanotransduction channel (Pan et al., 2018). In addition, truncated turtle TMC1/2 proteins when reconstituted into artificial lipid bilayers have been reported to form mechanically activated ion channels (Jia et al., 2020). While these studies await confirmation by structural studies and additional reconstitutions, they are consistent with the model that TMC1 and TMC2 contribute to the pore of the sensory mechanotransduction channel of cochlear hair cells. TMC1 has also been shown to be part of a leak channel in cochlear hair cells (Liu et al., 2019). Thus, TMC1 has been implicated to be a component of

at least two functionally distinct ion channels in hair cells. We observed widespread expression of TMC1 in hair cells, suggesting that its function is not confined to stereocilia.

Like TMC1/2, TMIE is essential for mechanotransduction by cochlear hair cells (Zhao et al., 2014). Since TMIE mutations affects the localization of TMC proteins to stereocilia of zebrafish hair cells, it has been proposed that TMIE is a transport protein or chaperone (Pacentine and Nicolson, 2019). While we confirm that TMIE affects the localization of TMC1, and to a lesser degree of TMC2, to stereocilia of mammalian hair cells, our findings suggest that the primary function of TMIE is not in protein transport. Instead, our findings are consistent with a model where TMIE is a subunit of the mechanotransduction channel in hair cells. These conclusions are based on sensitive biochemical and electrophysiological assays, which have revealed effects of TMIE mutations on the pore and gating properties of the mechanotransduction channel. Zebrafish TMIE mutations were evaluated by FM4–64 uptake into hair cells and by microphonics (Pacentine and Nicolson, 2019), assays of limited sensitivity that also cannot evaluate effects of mutations on single channel function. Defects in the localization of TMC1/2 proteins in *Tmie* mutants could be a consequence of defects in channel assembly that secondarily affect localization. This model has parallels in other biological systems. For example, the transport and conductance properties of glutamate receptors and voltage gated ion channels is regulated by ion channel subunits (Jackson and Nicoll, 2011; Yu and Catterall, 2004).

Our findings suggest that TMIE is a modular protein where the N- and C-terminal parts of the protein have distinct functions. TMIE contains two predicted TM domains (Mitchem et al., 2002; Naz et al., 2002). Deletion of the N-terminal region of TMIE including the first TM domain affects channel gating, which might be explained by perturbations in the interaction of TMIE with other components of the mechanotransduction complex such as LHFPL5 and the tip-link cadherins PCDH15, which bind to TMIE (Zhao et al., 2014). In this model, defects in channel gating could be a result of altered force transmission caused by improper coupling of the mechanotransduction channel to the tip link. In contrast, the C-terminal part of TMIE is critical for binding to TMC1/2 and for channel function. Deletion of 20 amino acids within the TMIE C-terminal cytoplasmic domain adjacent to the plasma membrane disrupt interactions of TMIE with TMC1/2 and are critical for the formation of a functional mechanotransduction channel. Point mutations in the N-terminal part of TMIE that are linked to deafness do not disrupt interactions of TMIE with TMC1/2 but affect the conductance and ion selectivity of the mechanotransduction channel, suggesting that TMIE is not just a linker protein but directly regulates the pore properties of the transduction channel.

We also provide evidence that the N-terminal cytoplasmic domain of TMIE mediates interactions with PIP_2, and that the point mutations linked to deafness affect PIP_2 binding. Studies in rats and frogs have shown that PIP_2 affects mechanotransduction including effects on channel resting open probability, conductance, ion selectivity and adaptation (Effertz et al., 2017; Hirono et al., 2004). We show here that PIP_2 affects mechanotransduction in OHCs of mice in similar ways. We reasoned that some of the PIP_2 effects might be mediated by TMIE.

Consistent with this model, mechanotransduction channels in hair cells from mice carrying the TMIE-R82C mutation are sensitized to PIP_2 depletion, leading to a faster decline of transducer currents upon prolonged PAO treatment compared to wild-type. This finding could be explained by reduced coupling of TMIE to PIP_2 in the plasma membrane. However, the R82C mutation may also affect mechantransduction in other ways. While the R82C mutation did not noticeably affect interactions with TMC1/2, it is within a domain that mediates interactions with TMC1/2. Perhaps, TMIE, TMC1/2 and PIP2 form a tight complex that is critical for channel function.

Notably, the R82C mutation is localized immediately next to the second transmembrane domain of TMIE. Modelling studies suggest that TMC1 contains a large pore that is partially open to the lipid environment (Ballesteros et al., 2018). Perhaps, the second transmembrane helix of TMIE associates with the predicted pore region of TMC1 and shields the pore from the lipid environment. In this model, the PIP_2 binding domain of TMIE is close to the pore region and thus appropriately localized to affect pore properties. In mechanically gated MscS channels and volume-regulated Swell channels, cytoplasmic protein domains interact with the pore to affect conductance properties of these channels (Wang et al., 2018; Zhou et al., 2018). The charged cytoplasmic domain of TREK-1 binds to phospholipids including PIP_2 and controls coupling of TREK-1 to the membrane and channel gating (Chemin et al., 2005; Chemin et al., 2007).

In conclusion, our data provide evidence that TMIE and TMC1/2 are subunits of the mechanotransduction channel in cochlear hair cells and that PIP_2 affects channel function at least in part via TMIE. It is tempting to speculate that the mechanotransduction channel contains additional subunits such as LHFPL5. Unfortunately, efforts have so far failed to reconstitute this mechanotransduction channel in heterologous cells (Cunningham and Muller, 2018; Qiu and Muller, 2018), which would permit additional biophysical experiments. TMC1 has also been shown to carry a leak current in hair cells (Liu et al., 2019) indicating additional functions for TMC1. Perhaps, TMC1/2 can form ion channels with different subcellular localizations and functions depending on the association with additional channel subunits.

STAR★METHODS

RESOURCE AVAILABILITY

Lead Contact—Further information and requests for resources and reagents should be directed to and will be fulfilled by the Lead Contact, Ulrich Mueller (umuelle3@jhmi.edu).

Materials Availability—Newly generated materials such as genetically modified mouse lines are available to qualified researchers upon request and after providing a signed MTA agreement.

Data and Code Availability—This study did not generate datasets and code.

EXPERIMENTAL MODEL AND SUBJECT DETAILS

Mouse strains—All animal experiments were approved by the Institutional Animal Care and Use Committee at Johns Hopkins University School of Medicine (#M016M271). Mice were maintained on a 14 hr. light/10 hr. dark cycle. Both male and female mice were used, and no obvious differences between the sexes were noted. All mice were group-housed in pathogen-free facilities with regulated temperature and humidity, and given *ad libitum* access to food and water. of the mice used were seemingly free of infection, health abnormalities, or immune system deficiencies. None of the mice used had been used for previous experiments. For all experiments except Auditory Brainstem Response (ABR) tests, mice were used at ages postnatal day 0 (P2) to P9. For ABR experiments, mice were ages 3–6 weeks. Mice from each strain were used as wild-type, heterozygous, or homozygous for the genetic modification and details are provided in the paper where appropriate. Controls for experiments were wild-type or heterozygous litter-mates.

Mice with loss-of-function alleles in *Tmie*, *Tmc1* and *Tmc2* have been described previously (*Tmie*$^{-/-}$ also referred to as *Tmie*^{LacZ}, (Zhao et al., 2014); *Tmc1*^{dn} also known as *Tmc1* deafness mutant (Kurima et al., 2002), *Tmc2*$^{-/-}$ (Kim et al., 2013)). CRISPR/Cas9 technology was used to generate *Tmc1-HA*, *Tmc2-Myc*, *Tmie-HA, Tmie-3X-Myc, Tmie-R82C* and *Tmie-R85W* mice. Exons were analyzed for potential sgRNA target sites using the website CRISPOR (crispor.tefor.net). Target sites were chosen based on proximity to desired genomic region and minimal number of predicted off-target sites. Target specific crRNA was ordered from Integrated DNA Technologies (IDT), along with tracrRNA. For both epitope-tagging and point mutations, ssDNAs containing desired insertions/mutations were designed containing 60 bp homology arms flanking the region of interest. ssDNAs also included silent mutations to PAM sites to prevent excessive cleavage by Cas9 after integration. Pronuclear injection of one-cell C57BL/6J embryos (Jackson Laboratories) was performed by the JHU Transgenic Core using standard microinjection techniques using a mix of Cas9 protein (30ng/ul, PNABio), tracrRNA (0.6μM, Dharmacon), crRNA (0.6μM, IDT) and ssDNA oligo (10ng/ul, IDT) diluted in RNAse free injection buffer (10 mM Tris-HCl, pH 7.4, 0.25 mM EDTA). Injected embryos were transferred into the oviducts of pseudopregnant ICR females (Envigo). Pseudopregnant mice were allowed to give birth, offspring resulting from embryo injections were tail-clipped at P21, and genomic DNA was collected. Genomic DNA was screened using PCR and sequencing to determine presence of insertions, deletions, or point mutations. Founder mice were bred with C57BL/6J mice (RRID:IMSR JAX:000664) and offspring were screened to verify germ-line transmission of mutations.

Genetic modifications for each strain:

Tmc1-HA: 5'-TACCCATACGATGTTCCAGATTACGCT-3' (encoding YPYDVPDYA) was inserted immediately before the endogenous stop codon of mouse *Tmc1*.

Tmc2-MYC: 5'-*GAACAAAAACTCATCTCAGAAGAGGATCTG-3'* (encoding EQKLISEEDL) was inserted immediately before the endogenous stop codon of mouse *Tmc2*.

Tmie-HA: 5’- *TACCCATACGATGTTCCAGATTACGCT*-3’ (encoding YPYDVPDYA) was inserted immediately before the endogenous stop codon of mouse *Tmie*.

Tmie-3X-MYC: 5’-*GGCGGCAGCGGCGAGCAGAAACTCATCTCTGAAGAAGATCTGGAACAAAAGTTG ATTTCA GAAGAAGATCTGGAACAGAAGCTCATCTCTGAGGAAGATCTG-3’* (encoding a 4 amino acid linker followed by three MYC tags—GGSGEQKLISEEDLEQKLISEEDLEQKLISEEDL) was inserted immediately before the endogenous stop codon of mouse *Tmie*.

Tmie-R82C: 5’-CGG-3’ encoding R82, was mutated to 5’-*TGC-3’*, encoding C82, of mouse *Tmie*.

Tmie-R85W: 5’-CGG-3’ encoding R85, was mutated to 5’-*TGG-3’*, encoding W85, of mouse *Tmie*.

Cell Lines—The HEK293 cell line used for heterologous expression was obtained from ATCC (#CRL-1573) and checked for mycoplasma contamination. Cells were grown at 37°C, 5% CO_2 in 1X DMEM+Glutamax (Gibco) containing 10% Fetal Bovine Serum and 1X Antibiotic-Antimycotic (Gibco). Cells used in experiments were passaged a maximum of twenty times.

METHOD DETAILS

Auditory Brainstem Response (ABR) measurements—ABR measurements were performed as described in (Schrode et al., 2018). Briefly, 3–6 week old mice were anesthetized with Ketamine (100mg/kg) and Xylazine (20 mg/kg) and placed on a heating pad inside of a sound attenuating chamber. Subdermal needle electrodes (E2, Grass Technologies, West Warwick, RI) were inserted on the left pinna, vertex, and on the leg (ground). ABR stimuli generation and signal acquisition were controlled by a custom MATLAB program interfacing TDT System 3 (Tucker-Davis Technology, Alachua, FL). ABR stimuli were delivered through a free-field speaker (FD28D, Fostex, Tokyo, Japan), placed 30 cm away from the animal’s head. ABR stimuli consisted of clicks and 5-ms tone pips of varying frequencies (8, 12, 16, 24, 32 kHz), and were presented in descending sound levels in 5 – 10 dB increments. ABR signals were amplified (ISO-80, Isolated Bio-Amplifier, World Precision Instruments, Sarasota, FL), band pass filtered 300–3000Hz (Krohn-Hite Model 3550, Krohn-Hite Corporation, Avon, MA), digitized (RX6 Multifunction Processor, TDT), and averaged across 300 presentations. ABR threshold was determined via ABR input/output function, as a stimulus level that produced peak-to peak ABR signal that was 2 standard deviations above the average background noise. ABR testing lasted approximately 40–60 min per mouse and the animal’s body temperature was closely monitored using a rectal temperature probe during test sessions. ABR data analysis was performed offline. Figures were generated using Origin Pro 7.5 (Origin Lab, Northampton, MA). Graph-Pad Prism 5 (Graph Pad Software, Inc., La Jolla, CA) was used for statistical analyses. All data is shown as mean ± SEM, unless otherwise noted.

Injectoporations of cochlear hair cells—Injectoporation experiments to express exogenous DNA in cochlear hair cells were carried out essentially as described (Cunningham et al., 2017; Xiong et al., 2012; Xiong et al., 2014; Zhao et al., 2014; Zhao et al., 2016). Briefly, the Organ of Corti was isolated from P3 wild-type and mutant mice and cultured as explants in 1X DMEM/F12 containing 1.5 μg/ml ampicillin. Various plasmid DNA constructs (0.5–1 μg/mL, described below) were injected in explants using glass pipettes (2 μm diameter) between rows of hair cells. Simultaneously with injection, explants were electroporated with four pulses at 60 V (15 msec pulse length, 1 sec inter-pulse intervals, ECM 830 square wave electroporator; BTX). After electroporation, media containing 10% fetal bovine serum was added to explants. Explants were incubated for 1–2 days at 37°C, 5% CO_2 before electrophysiology and/or immunostaining (see details below).

Electrophysiology—Mechanotransduction (MET) currents were recorded following our published procedures (Cunningham et al., 2017; Wu et al., 2017; Xiong et al., 2012; Zhao et al., 2014). During recording, apical perfusion was used to perfuse artificial perilymph (in mM): 144 NaCl, 0.7 NaH_2PO_4, 5.8 KCl, 1.3 $CaCl_2$, 0.9 $MgCl_2$, 5.6 glucose, and 10 H-HEPES, pH 7.4. Borosilicate glass with filament (Sutter, CA) was pulled with a P-2000 pipette puller (Sutter, CA), and polished with a MF-930 microforge (Narishige, Japan) to resistances of 2–3 MΩ. For mechanical stimulation, hair bundles were deflected with a glass probe mounted on a piezoelectric stack actuator (Thorlab, Newton, NJ). The actuator was driven by voltage steps that were low-pass filtered at a frequency of 10 KHz with a 900CT eight-pole Bessel filter (Frequency Devices) to diminish the resonance of the piezo stack. Whole-cell recordings were carried out and currents were sampled at 100 KHz with an EPC 10 USB patch-clamp amplifier (HEKA, Germany). To record macroscopic currents, the patch pipette was filled with intracellular solution (in mM): 140 mM KCl, 1 mM $MgCl_2$, 0.1 mM EGTA, 2 mM Mg-ATP, 0.3 mM Na-GTP and 10 mM H-HEPES, pH 7.2. Cells were voltage clamped at −74mV. Uncompensated series resistance was less than 5 MΩ. For single-channel recordings, we followed our published procedures (Xiong et al., 2012). Hair cells were briefly treated with Ca^{2+} free solution (144 mM NaCl, 0.7 mM NaH_2PO_4, 5.8 mM KCl, 5 mM EGTA, 0.9 mM $MgCl_2$, 5.6 mM glucose, and 10 mM H-HEPES, pH 7.4) by fluid jet to obtain single transducer channels. To measure single-channel currents, a −80 mV holding potential was applied; the intracellular solution consisted of 140 mM CsCl, 1 mM $MgCl_2$, 1 mM EGTA, 2 mM Mg-ATP, 0.3 mM Na-GTP and 10 mM H-HEPES, pH 7.2. For reversal potential measurements, the external solution consisted of 100 mM CaCl2, 20 N-methylglucamine, 6 mM Tris, 10 mM Glucose, pH 7.4. The liquid junction potential for the solutions in this study was corrected.

Phenylarsine oxide (PAO; Sigma-Aldrich) was dissolved in 100% DMSO as stock solution. Working solution with 100 μM PAO was freshly prepared before experiments. PAO was applied to the hair cells with an apical perfusion pipette (Effertz et al., 2017).

Whole-mount and explant immunohistochemistry and imaging—Whole mount cochleas or explants resulting from injectoporation from postnatal wildtype and mutant mice were dissected, fixed, and immunostained as described (Cunningham et al., 2017; Grillet et al., 2009). Briefly, for whole mounts, temporal bones were removed from the skull in 1x

HBSS containing 1.5 mM $CaCl_2$. Openings were made in the bony cochlear shell at the apex and through the oval and round windows. Temporal bones were incubated in 1x HBSS containing 4% PFA and 1.5 mM $CaCl_2$ for 30 minutes at RT with gentle agitation. For injectoporated explants, dishes containing explants were incubated with 1x HBSS containing 4% PFA and 1.5 mM $CaCl_2$ for 30 minutes at RT. Fixed tissues were washed in 1x PBS, the bony cochlear shell was removed, and the Organ of Corti was separated from the modiolus and collected for immunostaining (for whole mounts). Reissner's membrane and the Tectorial membrane were dissected away, and the Organ of Corti was permeabilized in PBS containing 10% Normal Goat Serum (GS) and 0.5% Triton for 30 minutes at RT with agitation. After permeabilization, the tissue was blocked in PBS containing 10% GS overnight at RT. The tissue was then incubated in PBS containing 10% GS and primary antibodies (see below) overnight at 4°C. The tissue was then washed three times in PBS and incubated for 1 hour at RT in PBS containing 10% GS, secondary antibodies (1:10000, Invitrogen, see below), and fluorescently-conjugated Phalloidin to label actin-rich stereocilia (Life Technologies, Phalloidin 405 Plus/488/555, 1:2000). After secondary antibody incubation, the tissue was washed three times and mounted on slides (whole-mounts) or coverslipped (explants) using ProLong Gold (Invitrogen). For tissues stained only for phalloidin, all steps were the same except for omission of primary antibody step. Tissues were imaged using 60x and 100x lenses on a widefield fluorescence deconvolution microscope (Deltavision, GE Life Sciences). For quantification of stereocilia bundle intensity after injectoporation, Z-stacks were taken of injectoporated hair cells encompassing the extent of the stereocilia and cell body. Individual image planes were selected from the apical cell body and from a region of the stereocilia when the hair bundle was in focus. Fluorescent intensity values were obtained from three unique regions of interest (ROIs) from selected cell body and stereocilia image planes using Deltavision Elite software. For each cell, ROIs were averaged for the cell body and the stereocilia, respectively, and then a ratio of stereocilia intensity/cell body intensity was calculated (referred to as "Intensity of Stereocilia Labeling). For each injectoporated construct, a mean value was calculated, and statistical significance was evaluated using a Students' t-test. IMARIS (version 9.3.1) was used to generate 3D reconstructions of phalloidin and TMC1/2 immunofluorescence.

Primary antibodies were as follows: rabbit anti-HA (1:500, Cell signaling, RRID: RRID:AB_1549585), rabbit anti-MYC (1:200, Cell Signaling, RRID:AB_490778), rabbit anti PCDH15-CD2 (1:500, (Webb et al., 2011)), rabbit anti-LHFPL5/TMHS (1:500, (Xiong et al., 2012), rabbit anti-CDH23 (1:500, (Kazmierczak et al., 2007; Siemens et al., 2004)) and rabbit anti-PMCA2 (1:200, Abcam, RRID:AB_303878).

Secondary antibodies were as follows: Goat anti-rabbit IgG F(ab')2, Alexa Fluor 488 (1:10000, Invitrogen, RRID:AB_2534114) and Goat anti-rabbit IgG F(ab'), Alexa Fluor 555 (1:10000, Invitrogen, RRID:AB_2535851).

Co-immunoprecipitation and western blotting—Co-immunoprecipitations were performed as described (Cunningham et al., 2017; Zhao et al., 2014; Zhao et al., 2016). Briefly, HEK293 cells were transfected with various plasmids using Lipofectamine 3000 (ThermoFisher). After 48 hours, cells were lysed using a modified RIPA buffer containing 150 mM NaCl, 50 mM Tris (pH 8), 1% NP-40, 0.5% Sodium Deoxycholate, 0.1% Sodium

Dodecyl Sulfate (SDS) and a Roche Complete Protease Inhibitor Tablet. After lysis, lysates were rotated for 30 minutes at 4°C followed by centrifugation at 20000 rcf for 15 minutes at 4°C. At this point, 10% of the lysate was set aside for use as an input control. The rest of the lysate was immunoprecipitated for 1 hour at 4°C using EZ View Red HA Affinity Gel (Sigma-Aldrich Cat# E6779, RRID:AB_10109562) or EZ View Red Flag M2 Affinity Gel ((Sigma-Aldrich Cat# F2426, RRID:AB_2616449). After immunoprecipitation, the affinity gel was washed three times with lysis buffer and mixed with 4x Bolt LDS Sample Buffer (Life Technologies) containing 10x Bolt Sample Reducing Agent (Life Technologies) to elute protein complexes. Eluted immunoprecipitated protein was run in parallel with input lysate on 4–12% Bolt Bis-Tris plus gels (Life Technologies) in Bolt MOPS Running Buffer (Life Technologies) and transferred to PVDF membranes for 1 hour at 4°C using the Mini Blot Module containing Bolt transfer buffer (Life technologies) with 10% Methanol. Membranes were blocked for 1 hour with 2% ECL Prime blocking reagent (GE Life Sciences) in 1X TBST (containing 20 mM Tris-HCl pH 7.5, 150 mM NaCl and 0.1% Tween-20). Membranes were incubated with primary antibodies (see below) in 2% ECL Prime in 1X TBST at 4° C overnight. After primary antibody incubation, membranes were washed three times with 1X TBST, followed by incubation for 1 hour at RT in ECL Prime solution containing secondary antibodies (see below) in 1X TBST. Membranes were washed three times in 1X TBST and then imaged with Clarity Substrate (Biorad) on a G-Box ECL imager (Syngene). Quantification of CoIP experiments was done using ImageJ and Microsoft Excel. Western blot band intensity values were obtained using ImageJ for IP bands and whole cell lysate bands for both IP and CoIP proteins. For each experiment, CoIP intensity values were normalized for expression and immunoprecipitation efficacy and divided by controls to generate relative CoIP Intensity values. Mean relative CoIP intensity values were calculated by combining relative values for each construct across independent experiments. For each construct, a mean value was calculated, and statistical significance relative to control constructs were evaluated using a Students' t-test.

Primary antibodies were as follows: mouse anti-Flag M2 (1:500, Sigma, RRID:AB_262044), rabbit anti-MYC (1:500, Cell Signaling, RRID:AB_490778), and rabbit anti-HA (1:500, Cell signaling, RRID: RRID:AB_1549585).

Secondary antibodies were Veriblot (1:5000, Abcam) and Veriblot anti-mouse (1:5000, Abcam).

Lipid strip binding—Membrane Lipid strips (P-6002) and PIP strips (P-6001) were obtained from Echelon Biosciences. Each strip contained 16 spots with 100 pmol of unique lipids on nitrocellulose membranes. Strips were blocked for 30 mins at RT with 3% BSA in 1X TBST or 1X TBST alone. Strips were incubated for 30 mins at RT with 0.5 μg/mL human TMIE (full length recombinant protein, NM_147196, purchased from Origene), 0.5 μg/mL GST-tagged PI(4.5)P_2 GRIP (the phospholipase C-δ1 PH domain, G-4501 Echelon Biosciences) or 25–50 μg/mL synthetic HA-tagged peptides encompassing various regions of the TMIE C-terminal cytoplasmic domain (see below for synthesis details). After protein/peptide incubation, strips were washed three times in 1X TBST. Strips were then incubated for 30 mins at RT with primary antibodies (see below) in 3% BSA/1X TBST or 1X TBST. Strips were washed for three times in 1X TBST and incubated for 30 minutes with Veriblot

in 1X TBST (1:5000, Abcam) for secondary antibody. Following secondary antibody incubation, strips were washed three times in 1X TBST and then imaged with Clarity Substrate (Biorad) on a G-Box ECL imager (Syngene). Quantification of lysis experiments was done using ImageJ and Microsoft Excel. For each membrane, lipid spot intensities were quantified using ImageJ, and each lipid spot was normalized to the intensity of phosphatidic acid binding intensity. Each peptide experiment was repeated at least three times, and normalized binding intensities were averaged across experiments.

Primary antibodies were as follows: rabbit anti TMIE (1:500, Sigma, RRID:AB_10675792), rabbit anti-HA (1:500, Cell signaling, RRID: RRID:AB_1549585, and rabbit anti-GST(1:500, Cell signaling, RRID:AB_490796).

Secondary antibodies were Veriblot (1:5000, Abcam).

DNA constructs and plasmids—DNA constructs were generated as described below. All constructs were sequence-verified.

TMIE and ARF6 Constructs: Expression vectors for pN3-TMIE-HA were described previously (Zhao et al., 2014). TMIE and ARF6 constructs were generated in a modified backbone derived from pEGFP-N3 with EGFP removed and containing a CMV-promoter (Zhao et al., 2014). We refer to this backbone as “pN3”. All constructs were generated by PCR-cloning using primers containing restriction enzyme sites, epitope tags, and extra nucleotides to allow for restriction digest. Inserts were subcloned into pN3 by digesting pN3 with SalI and NotI restriction enzyme sites, except for pN3-TMIE-28–153-HA (used HindIII and NotI). Specific details for each construct are below.

pN3-TMIE-11–153-HA: pN3-TMIE-HA was used as a PCR template to generate TMIE-11–153-HA. Primers were (i) 5’-*AAAAAAGTCGACGCCACCATGTGGGCGCTGGG*-3’; and (ii): 5’-*AAAAAAGCGGCCGCTCAAGCGTAATCTGGAACATC*-3’.

pN3-TMIE-28–153-HA: pN3-TMIE-HA was used as a PCR template to generate TMIE-28–153-HA. Primers were (i) 5’- *GCTAAAGCTTATGACGCAGCTGGTAGAGCCCAGC*-3’; and (ii): 5’-*GTGCGGCCGCTCAAGCGTAATCTGGAACATCGTATGGGTACATTTTCTCTCCTTTCTT*-3’ pN3-TMIE-CDTM-HA: TMIE-CDTM-HA had the first predicted transmembrane(TM) domain of TMIE replaced with the predicted TM domain from CD6 (DNA sequence: 5’-*CTTCTCATTCTCTGTATTGTCCTGGGAATTCTCCTCCTCGTCTCCACCATCTTCATAGTTATT*-3’, Amino acid sequence: LLILCIVLGILLLVSTIFIVI) and the second predicted TM domain of TMIE replaced with the predicted TM domain from CD7 (DNA sequence: 5’-*GCTGCCATTGCTGTAGGCTTCTTCTTCACCGGGCTGCTCCTTGGGGTGGTGTGCAGCATG CTG*-3’ Amino acid sequence: AAIAVGFFFTGLLLGVVCSML). The entire construct (SalI-TMIE-CD6TM-TMIE-CD7TM-TMIE-HA-NotI) was synthesized as a gBlock gene fragment from IDT and cloned into pN3.

pN3-TMIEdel80–100-HA: Overlap PCR cloning was used to generate TMIE-del80–100-HA. pN3-TMIE-HA was used as a PCR template for initial reactions, and then PCR products from initial reactions were used as templates for final reaction. Primers were (i) 5'-*TCTGCAGTCGACATGGCCGGGAGGCAG*-3'; (ii): 5-*AGCTTGTCTGTGTACATCTTGAAGACACAGCATAGCGTGATGAT*-3'. (iii) 5'-*TCACGCTATGCTGTGTCTTCAAGATGTACACAGACAAGCTGGAGACT*-3'. (iv) 5'-*AGAGTCGCGGCCGCTCAAGCGTAATCTGGAACATCGTATGGGTATTTCTCTCCTTTCTTCTTGGCCTC*-3'

pN3-TMIEdel101–121-HA: Overlap PCR cloning was used to generate TMIE-del101–121-HA. pN3-TMIE-HA was used as a PCR template for initial reactions, and then PCR products from initial reactions were used as templates for final reaction. Primers were (i) 5'-*TCTGCAGTCGACATGGCCGGGAGGCAG*-3'; (ii): 5-*TTCTTTTTCTTCTTGTCCTCGGCCGCCTTTCGCTGTA*-3'. (iii) 5'-*ATCTACAGCGAAAGGCGGCCGAGGACAAGAAGAAAAAGAAGAAGGACA*-3'. (iv) 5'-*AGAGTCGCGGCCGCTCAAGCGTAATCTGGAACATCGTATGGGTATTTCTCTCCTTTCTTCTTGGCCTC*-3'

pN3-TMIEdel122–142-HA: Overlap PCR cloning was used to generate TMIE-del122–142-HA. pN3-TMIE-HA was used as a PCR template for initial reactions, and then PCR products from initial reactions were used as templates for final reaction. Primers were (i) 5'-*TCTGCAGTCGACATGGCCGGGAGGCAG*-3'; (ii): 5-*TTCTTGGCCTCATTCTTCTCTCCAGGGATTTCTGTGAGTTCATTA*-3'. (iii) 5'-*AACTCACAGAAATCCCTGGAGAGAAGAATGAGGCCAAGAAGAAAG*-3'. (iv) 5'-*AGAGTCGCGGCCGCTCAAGCGTAATCTGGAACATCGTATGGGTATTTCTCTCCTTTCTTCTTGGCCTC*-3'

TMC1, TMC2 and ARF6 constructs: To maximize TMC1/2 expression, we generated TMC1/2 constructs in pCAGEN (Addgene #11160), containing a CAG promoter that has been previously used for strong mammalian expression. All constructs were generated using PCR-cloning with primers containing restriction enzyme sites, epitope tags, and extra nucleotides to allow for restriction digest. pCAGEN and inserts were digested with enzymes specified below with each construct.

pCAGEN-MYC-TMC1: pN3-MYC-TMC1 (Zhao et al., 2014) was used as a PCR template to generate MYC-TMC1. PCR primers were (i) 5'-*AAAAAAGCGGCCGCGCCACCATGGAACAAAAACTCATCTCAGAAGAGG*-3'; and (ii): 5' *AAAAAAGCGGCCGCTTACTGGCCACCAGCAGC*-3'. pCAGEN and insert were digested with NotI.

pCAGEN-TMC1-HA: pN3-MYC-TMC1 (Zhao et al., 2014) was used as a PCR template to generate TMC1-HA. PCR primers were (i) 5'-*GATATCGCGGCCGCGCCACCATGTTGCAAATCCAAGTGGAG*-3'; and (ii): 5' *AGGAGTGCGGCCGCTTAAGCGTAATCTGGAACATCGTATGGGTACTGGCCACCAGCAGCT*-3'. pCAGEN and insert were digested with NotI.

pCAGEN-MYC-TMC2: pN3-MYC-TMC2 (Zhao et al., 2014) was used as a PCR template to generate MYC-TMC2. PCR primers were (i) 5'-*AAAAAACAATTGGCCACCATGGAACAAAAACTCATCTCAGAAGAGG*-3'; and (ii): 5' *AAAAAAAAGCGGCCGCTCAGTTGTGAGGCCTCTGG*-3'. pCAGEN was digested with EcoRI/NotI, and the insert was digested with MfeI (compatible with EcoRI)/NotI.

pCAGEN-TMC2-MYC: pN3-MYC-TMC2 (Zhao et al., 2014) was used as a PCR template to generate TMC2-MYC. PCR primers were (i) 5'-*GATATCGCGGCCGCGCCACCATGAGCCCCCAGTTAAAGAGC*-3'; and (ii): 5' *AGGAGTGCGGCCGCTCACAGATCCTCTTCTGAGATGAGTTTCTGCTCGTTGTGAG GCCTCTGGGTT*-3'. pCAGEN and insert were digested with NotI.

pCAGEN-TMC1-FLAG: pN3-MYC-TMC1 (Zhao et al., 2014) was used as a PCR template to generate TMC1-FLAG. PCR primers were (i) 5'-*AAAAAAAAGCGGCCGCGCCACCATGTTGCAAATCCAAGTGGAG*-3'; and (ii): 5' *AAAAAAAAGCGGCCGCTTACTTGTCGTCATCGTCTTTGTAGTCCTGGCCACCAGC AGCTG*-3'. pCAGEN and insert were digested with NotI.

pCAGEN-TMC2-FLAG: pN3-MYC-TMC2 (Zhao et al., 2014) was used as a PCR template to generate TMC2-FLAG. PCR primers were (i) 5'-*AAAAAAAAGCGGCCGCGCCACCATGAGCCCCCAGTTAAAGAGC*-3'; and (ii): 5' *AAAAAAAAGCGGCCGCTCACTTGTCGTCATCGTCTTTGTAGTCGTTGTGAGGCCT CTGGGTTC*-3'. pCAGEN and insert were digested with NotI.

pCAGEN-MYC-ARF6: Mouse cochlear cDNA was used as a PCR template to amplify mouse *Arf6* coding sequence and generate MYC-ARF6. PCR primers were (i) 5' *AAAAAAAAGAATTCGCCACCATGGAACAAAAACTCATCTCAGAAGAGGATCTGG GGAAGGTGCTATCCAAGATCT*-3'; and (ii): 5' *AAAAAAAAGCGGCCGCTTAGGATTTGTAGTTAGAGGTTAACCATGT*-3'. Insert and pCAGEN were digested with EcoRI and NotI.

Peptide synthesis—Wildtype and mutant HA-tagged peptides encompassing portions of the TMIE C-terminal cytoplasmic domain were synthesized by the Johns Hopkins University Synthesis and Sequencing Facility on an Aapptec Focus XC synthesizer utilizing Fmoc chemistry. The peptides were purified using reversed-phase HPLC on a Waters XBridge peptide BEH C18 column. The resulting fractions were checked using MALDI-TOF mass spectrometry for the correct molecular weight and pure fractions were pooled and lyophilized.

QUANTIFICATION AND STATISTICAL ANALYSIS

Data analysis was performed using Excel (Microsoft) and Igor pro 7 (WaveMetrics, Lake Oswego, OR).Transduction current-displacement curves (I(X)) were fitted with the following double Boltzmann (Peng et al., 2013; Peng et al., 2016):

$$I(x) = \frac{I_{max}}{1 + e^{z1(x_0 - x)}\left(1 + e^{z2(x_0 - x)}\right)}$$

Where Z_1 and Z_2 are the slope factors and x_0 represents the set point.

Current/Voltage plots were fitted with A single-site binding model (Effertz et al., 2017; Kros et al., 1992; Farris et al., 2004).

The relative Ca2+ permeability, P_{Ca}/P_{Cs}, was calculated from the Goldman-Hodgkin-Katz equation (Kim and Fettiplace, 2013, Kim et al., 2013)

Statistical details are described in the Results, Figures and Figure Legends. All data are mean ± SEM. Student's two-tailed unpaired t test was used to determine statistical significance for two group comparisons (*, $p<0.05$, **, $p<0.01$, ***, $p<0.001$, ****, $p<0.0001$). Exact values of n are reported where appropriate. Depending on the experiment, n represents number of animals, number of cells, or number of experiments.

Supplementary Material

Refer to Web version on PubMed Central for supplementary material.

Acknowledgements

We thank members of the laboratory for comments and criticisms and Angela Ballesteros for helpful suggestions. We are grateful to Michelle Monroe and Kaiping Zhang for assistance with mouse genotyping. We thank Chip Hawkins and the Johns Hopkins Transgenic Mouse Core for help generating mouse mutants; Jodie Franklin and the Johns Hopkins University Synthesis and Sequencing Facility for DNA sequencing and peptide synthesis; Michele Pucak and the Johns Hopkins Department of Neuroscience Multiphoton Imaging Core for assistance with IMARIS. This work was supported by the NIH (C.C.; F32DC015724; Z.W.; K99DC016328; U.M.; RO1DC005965, RO1DC007704, RO1DC014713, RO1DC016960) and the David M. Rubenstein Fund for Hearing Research. U.M. is a Bloomberg Distinguished Professor for Neuroscience and Biology.

REFERENCES

Assad JA, Shepherd GM, and Corey DP (1991). Tip-link integrity and mechanical transduction in vertebrate hair cells. Neuron 7, 985–994. [PubMed: 1764247]

Ballesteros A, Fenollar-Ferrer C, and Swartz KJ (2018). Structural relationship between the putative hair cell mechanotransduction channel TMC1 and TMEM16 proteins. eLife 7.

Basu A, Lagier S, Vologodskaia M, Fabella BA, and Hudspeth AJ (2016). Direct mechanical stimulation of tip links in hair cells through DNA tethers. eLife 5.

Beurg M, Cui R, Goldring AC, Ebrahim S, Fettiplace R, and Kachar B (2018). Variable number of TMC1-dependent mechanotransducer channels underlie tonotopic conductance gradients in the cochlea. Nat Commun 9, 2185. [PubMed: 29872055]

Beurg M, Evans MG, Hackney CM, and Fettiplace R (2006). A large-conductance calcium-selective mechanotransducer channel in mammalian cochlear hair cells. J Neurosci 26, 10992–11000. [PubMed: 17065441]

Beurg M, Fettiplace R, Nam JH, and Ricci AJ (2009). Localization of inner hair cell mechanotransducer channels using high-speed calcium imaging. Nat Neurosci.

Beurg M, Goldring AC, and Fettiplace R (2015a). The effects of Tmc1 Beethoven mutation on mechanotransducer channel function in cochlear hair cells. The Journal of general physiology 146, 233–243. [PubMed: 26324676]

Beurg M, Kim KX, and Fettiplace R (2014). Conductance and block of hair-cell mechanotransducer channels in transmembrane channel-like protein mutants. The Journal of general physiology 144, 55–69. [PubMed: 24981230]

Beurg M, Xiong W, Zhao B, Muller U, and Fettiplace R (2015b). Subunit determination of the conductance of hair-cell mechanotransducer channels. Proc Natl Acad Sci U S A 112, 1589–1594. [PubMed: 25550511]

Chemin J, Patel AJ, Duprat F, Lauritzen I, Lazdunski M, and Honore E (2005). A phospholipid sensor controls mechanogating of the K+ channel TREK-1. EMBO J 24, 44–53. [PubMed: 15577940]

Chemin J, Patel AJ, Duprat F, Sachs F, Lazdunski M, and Honore E (2007). Up- and down-regulation of the mechano-gated K(2P) channel TREK-1 by PIP (2) and other membrane phospholipids. Pflugers Arch 455, 97–103. [PubMed: 17384962]

Corns LF, Jeng JY, Richardson GP, Kros CJ, and Marcotti W (2017). TMC2 Modifies Permeation Properties of the Mechanoelectrical Transducer Channel in Early Postnatal Mouse Cochlear Outer Hair Cells. Front Mol Neurosci 10, 326. [PubMed: 29093662]

Corns LF, Johnson SL, Kros CJ, and Marcotti W (2016). Tmc1 Point Mutation Affects Ca2+ Sensitivity and Block by Dihydrostreptomycin of the Mechanoelectrical Transducer Current of Mouse Outer Hair Cells. J Neurosci 36, 336–349. [PubMed: 26758827]

Cunningham CL, and Muller U (2018). Molecular Structure of the Hair Cell Mechanoelectrical Transduction Complex. Cold Spring Harb Perspect Med.

Cunningham CL, Wu Z, Jafari A, Zhao B, Schrode K, Harkins-Perry S, Lauer A, and Muller U (2017). The murine catecholamine methyltransferase mTOMT is essential for mechanotransduction by cochlear hair cells. eLife 6.

D'Souza-Schorey C, van Donselaar E, Hsu VW, Yang C, Stahl PD, and Peters PJ (1998). ARF6 targets recycling vesicles to the plasma membrane: insights from an ultrastructural investigation. J Cell Biol 140, 603–616. [PubMed: 9456320]

Delmas P, and Coste B (2013). Mechano-gated ion channels in sensory systems. Cell 155, 278–284. [PubMed: 24120130]

Effertz T, Becker L, Peng AW, and Ricci AJ (2017). Phosphoinositol-4,5-Bisphosphate Regulates Auditory Hair-Cell Mechanotransduction-Channel Pore Properties and Fast Adaptation. J Neurosci 37, 11632–11646. [PubMed: 29066559]

Farris HE, LeBlanc CL, Goswami J, and Ricci AJ (2004). Probing the pore of the auditory hair cell mechanotransducer channel in turtle. J Physiol 558, 769–792. [PubMed: 15181168]

Ge J, Elferich J, Goehring A, Zhao H, Schuck P, and Gouaux E (2018). Structure of mouse protocadherin 15 of the stereocilia tip link in complex with LHFPL5. eLife 7.

Grillet N, Xiong W, Reynolds A, Kazmierczak P, Sato T, Lillo C, Dumont RA, Hintermann E, Sczaniecka A, Schwander M, et al. (2009). Harmonin mutations cause mechanotransduction defects in cochlear hair cells. Neuron 62, 375–387. [PubMed: 19447093]

Hirono M, Denis CS, Richardson GP, and Gillespie PG (2004). Hair cells require phosphatidylinositol 4,5-bisphosphate for mechanical transduction and adaptation. Neuron 44, 309–320. [PubMed: 15473969]

Jackson AC, and Nicoll RA (2011). The expanding social network of ionotropic glutamate receptors: TARPs and other transmembrane auxiliary subunits. Neuron 70, 178–199. [PubMed: 21521608]

Jia Y, Zhao Y, Kusakizako T, Wang Y, Pan C, Zhang Y, Nureki O, Hattori M, and Yan Z (2020). TMC1 and TMC2 Proteins Are Pore-Forming Subunits of Mechanosensitive Ion Channels. Neuron 105, 310–321 e313. [PubMed: 31761710]

Kawashima Y, Geleoc GS, Kurima K, Labay V, Lelli A, Asai Y, Makishima T, Wu DK, Della Santina CC, Holt JR, et al. (2011). Mechanotransduction in mouse inner ear hair cells requires transmembrane channel-like genes. J Clin Invest 121, 4796–4809. [PubMed: 22105175]

Kazmierczak P, Sakaguchi H, Tokita J, Wilson-Kubalek EM, Milligan RA, Muller U, and Kachar B (2007). Cadherin 23 and protocadherin 15 interact to form tip-link filaments in sensory hair cells. Nature 449, 87–91. [PubMed: 17805295]

Kim KX, Beurg M, Hackney CM, Furness DN, Mahendrasingam S, and Fettiplace R (2013). The role of transmembrane channel-like proteins in the operation of hair cell mechanotransducer channels. The Journal of general physiology 142, 493–505. [PubMed: 24127526]

Kim KX, and Fettiplace R (2013). Developmental changes in the cochlear hair cell mechanotransducer channel and their regulation by transmembrane channel-like proteins. The Journal of general physiology 141, 141–148. [PubMed: 23277480]

Kros CJ, Rusch A, and Richardson GP (1992). Mechano-electrical transducer currents in hair cells of the cultured neonatal mouse cochlea. Proc Biol Sci 249, 185–193. [PubMed: 1280836]

Kurima K, Ebrahim S, Pan B, Sedlacek M, Sengupta P, Millis BA, Cui R, Nakanishi H, Fujikawa T, Kawashima Y, et al. (2015). TMC1 and TMC2 Localize at the Site of Mechanotransduction in Mammalian Inner Ear Hair Cell Stereocilia. Cell reports 12, 1606–1617. [PubMed: 26321635]

Kurima K, Peters LM, Yang Y, Riazuddin S, Ahmed ZM, Naz S, Arnaud D, Drury S, Mo J, Makishima T, et al. (2002). Dominant and recessive deafness caused by mutations of a novel gene, TMC1, required for cochlear hair-cell function. Nat Genet 30, 277–284. [PubMed: 11850618]

Lee SJ, Weller E, Alyea EP, Ritz J, and Soiffer RJ (1998). Efficacy and costs of granulocyte colony-stimulating factor in allogeneic T-cell depleted bone marrow transplantation. Blood 92, 2725–2729. [PubMed: 9763556]

Liu S, Wang S, Zou L, Li J, Song C, Chen J, Hu Q, Liu L, and Xiong W (2019). TMC1 confers a leak conductance to modulate excitability of auditory hair cells in mammals. BioRXiv.

Maeda R, Kindt KS, Mo W, Morgan CP, Erickson T, Zhao H, Clemens-Grisham R, Barr-Gillespie PG, and Nicolson T (2014). Tip-link protein protocadherin 15 interacts with transmembrane channel-like proteins TMC1 and TMC2. Proc Natl Acad Sci U S A 111, 12907–12912. [PubMed: 25114259]

Mahendrasingam S, Fettiplace R, Alagramam KN, Cross E, and Furness DN (2017). Spatiotemporal changes in the distribution of LHFPL5 in mice cochlear hair bundles during development and in the absence of PCDH15. PLoS One 12, e0185285. [PubMed: 29069081]

Mitchem KL, Hibbard E, Beyer LA, Bosom K, Dootz GA, Dolan DF, Johnson KR, Raphael Y, and Kohrman DC (2002). Mutation of the novel gene Tmie results in sensory cell defects in the inner ear of spinner, a mouse model of human hearing loss DFNB6. Hum Mol Genet 11, 1887–1898. [PubMed: 12140191]

Naz S, Giguere CM, Kohrman DC, Mitchem KL, Riazuddin S, Morell RJ, Ramesh A, Srisailpathy S, Deshmukh D, Riazuddin S, et al. (2002). Mutations in a novel gene, TMIE, are associated with hearing loss linked to the DFNB6 locus. Am J Hum Genet 71, 632–636. [PubMed: 12145746]

Ohmori H (1985). Mechano-electrical transduction currents in isolated vestibular hair cells of the chick. J Physiol 359, 189–217. [PubMed: 2582113]

Orta-Mascaro M, Consuegra-Fernandez M, Carreras E, Roncagalli R, Carreras-Sureda A, Alvarez P, Girard L, Simoes I, Martinez-Florensa M, Aranda F, et al. (2016). CD6 modulates thymocyte selection and peripheral T cell homeostasis. J Exp Med 213, 1387–1397. [PubMed: 27377588]

Pacentine IV, and Nicolson T (2019). Subunits of the mechano-electrical transduction channel, Tmc1/2b, require Tmie to localize in zebrafish sensory hair cells. PLoS Genet 15, e1007635. [PubMed: 30726219]

Pan B, Akyuz N, Liu XP, Asai Y, Nist-Lund C, Kurima K, Derfler BH, Gyorgy B, Limapichat W, Walujkar S, et al. (2018). TMC1 Forms the Pore of Mechanosensory Transduction Channels in Vertebrate Inner Ear Hair Cells. Neuron 99, 736–753 e736. [PubMed: 30138589]

Pan B, Geleoc GS, Asai Y, Horwitz GC, Kurima K, Ishikawa K, Kawashima Y, Griffith AJ, and Holt JR (2013). TMC1 and TMC2 are components of the mechanotransduction channel in hair cells of the mammalian inner ear. Neuron 79, 504–515. [PubMed: 23871232]

Peng AW, Effertz T, and Ricci AJ (2013). Adaptation of mammalian auditory hair cell mechanotransduction is independent of calcium entry. Neuron 80, 960–972. [PubMed: 24267652]

Peng AW, Gnanasambandam R, Sachs F, and Ricci AJ (2016). Adaptation Independent Modulation of Auditory Hair Cell Mechanotransduction Channel Open Probability Implicates a Role for the Lipid Bilayer. J Neurosci 36, 2945–2956. [PubMed: 26961949]

Qiu X, and Muller U (2018). Mechanically Gated Ion Channels in Mammalian Hair Cells. Front Cell Neurosci 12, 100. [PubMed: 29755320]

Ranade SS, Syeda R, and Patapoutian A (2015). Mechanically Activated Ion Channels. Neuron 87, 1162–1179. [PubMed: 26402601]

Ricci AJ, Crawford AC, and Fettiplace R (2003). Tonotopic variation in the conductance of the hair cell mechanotransducer channel. Neuron 40, 983–990. [PubMed: 14659096]

Schrode KM, Muniak MA, Kim YH, and Lauer AM (2018). Central Compensation in Auditory Brainstem after Damaging Noise Exposure. eNeuro 5.

Siemens J, Lillo C, Dumont RA, Reynolds A, Williams DS, Gillespie PG, and Muller U (2004). Cadherin 23 is a component of the tip link in hair-cell stereocilia. Nature 428, 950–955. [PubMed: 15057245]

Wang X, Tang S, Wen X, Hong L, Hong F, and Li Y (2018). Transmembrane TM3b of Mechanosensitive Channel MscS Interacts With Cytoplasmic Domain Cyto-Helix. Front Physiol 9, 1389. [PubMed: 30327617]

Webb SW, Grillet N, Andrade LR, Xiong W, Swarthout L, Della Santina CC, Kachar B, and Muller U (2011). Regulation of PCDH15 function in mechanosensory hair cells by alternative splicing of the cytoplasmic domain. Development 138, 1607–1617. [PubMed: 21427143]

Wu Z, Grillet N, Zhao B, Cunningham C, Harkins-Perry S, Coste B, Ranade S, Zebarjadi N, Beurg M, Fettiplace R, et al. (2017). Mechanosensory hair cells express two molecularly distinct mechanotransduction channels. Nat Neurosci 20, 24–33. [PubMed: 27893727]

Xiang M, Gao WQ, Hasson T, and Shin JJ (1998). Requirement for Brn-3c in maturation and survival, but not in fate determination of inner ear hair cells. Development 125, 3935–3946. [PubMed: 9735355]

Xiong W, Grillet N, Elledge HM, Wagner FJ, Zhao B, Johnson KR, Kazmierczak P, and Müller U (2012). TMHS is an integral component of the mechanotransduction machinery of cochlear hair cells. Cell 151.

Xiong W, Wagner T, Yan L, Grillet N, and Muller U (2014). Using injectoporation to deliver genes to mechanosensory hair cells. Nature protocols 9, 2438–2449. [PubMed: 25232939]

Yu FH, and Catterall WA (2004). The VGL-chanome: a protein superfamily specialized for electrical signaling and ionic homeostasis. Sci STKE 2004, re15. [PubMed: 15467096]

Yue X, Zhao J, Li X, Fan Y, Duan D, Zhang X, Zou W, Sheng Y, Zhang T, Yang Q, et al. (2018). TMC Proteins Modulate Egg Laying and Membrane Excitability through a Background Leak Conductance in C. elegans. Neuron 97, 571–585 e575. [PubMed: 29395910]

Zaoui K, Rajadurai CV, Duhamel S, and Park M (2019). Arf6 regulates RhoB subcellular localization to control cancer cell invasion. J Cell Biol 218, 3812–3826. [PubMed: 31591185]

Zhao B, Wu Z, Grillet N, Yan L, Xiong W, Harkins-Perry S, and Muller U (2014). TMIE Is an Essential Component of the Mechanotransduction Machinery of Cochlear Hair Cells. Neuron 84, 954–967. [PubMed: 25467981]

Zhao B, Wu Z, and Muller U (2016). Murine Fam65b forms ring-like structures at the base of stereocilia critical for mechanosensory hair cell function. eLife 5.

Zhao Y, Yamoah EN, and Gillespie PG (1996). Regeneration of broken tip links and restoration of mechanical transduction in hair cells. Proc Natl Acad Sci U S A 93, 15469–15474. [PubMed: 8986835]

Zhou P, Polovitskaya MM, and Jentsch TJ (2018). LRRC8 N termini influence pore properties and gating of volume-regulated anion channels (VRACs). J Biol Chem 293, 13440–13451. [PubMed: 29925591]

Highlights

- TMC1/2 cannot form functional mechanotransduction channels in hair cells without TMIE
- TMIE is a subunit of the mechanotransduction channel of cochlear hair cells
- TMIE mutations affect pore properties such as conductance and ion selectivity
- TMIE binds PIP_2 and deafness mutations affect PIP_2 binding and transduction

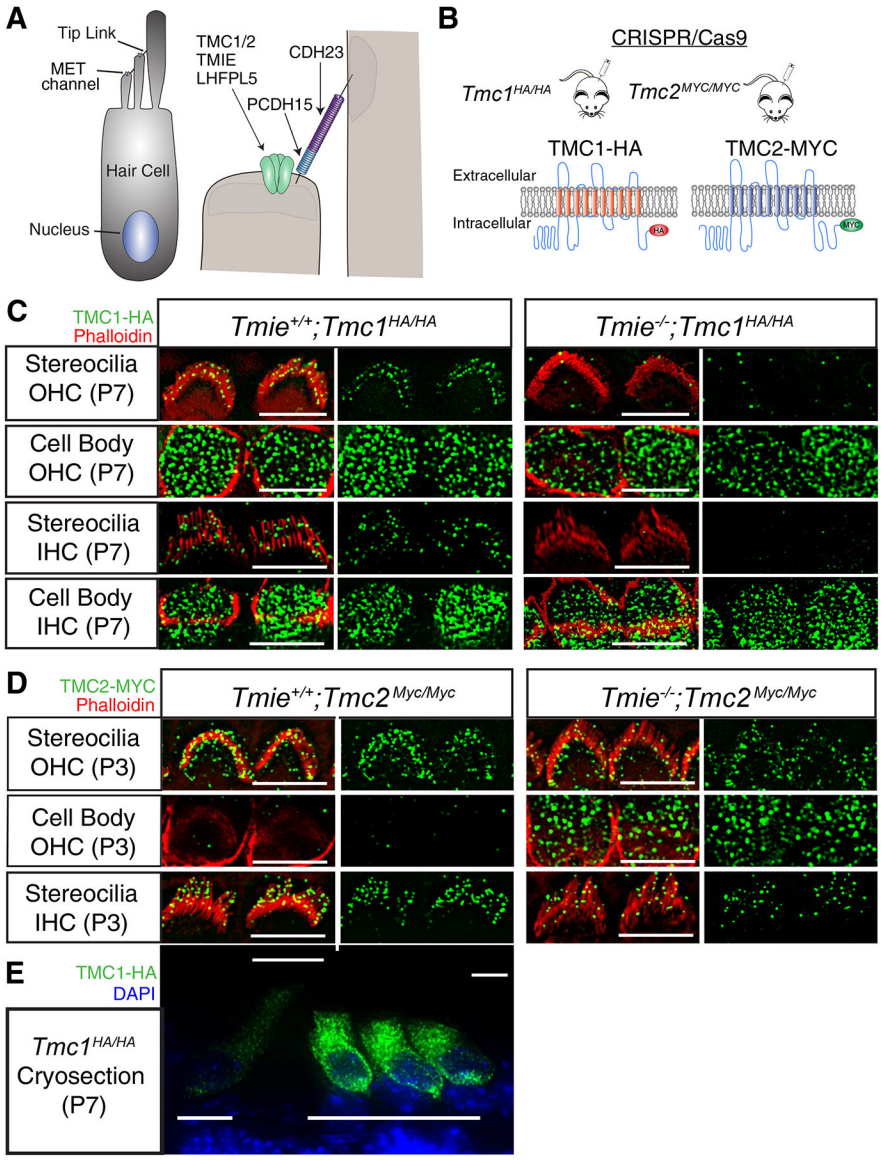

Figure 1. Effects of TMIE on TMC1-HA and TMC2-MYC localization.

(A) Diagram of a hair cell and the mechanotransduction complex at tip links. (B) Schematic of generation of mouse strains with epitope-tag endogenous TMC1 and TMC2. (C) OHCs and IHCs from P7 *Tmc1*$^{HA/HA}$ mice immunostained in whole mounts for HA (green) and phalloidin (red) to label stereocilia in the presence (*Tmie*$^{+/+}$;*Tmc1*$^{HA/HA}$, left panels) or absence (*Tmie*$^{-/-}$;*Tmc1*$^{HA/HA}$, right panels) of *Tmie*. (D) OHCs and IHCs from P3 *Tmc2*$^{MYC/MYC}$ mice immunostained in whole mounts for MYC (green) and phalloidin (red). (E) Cryosection from P7 *Tmc1*$^{HA/HA}$ cochlea immunostained for HA (green) and DAPI (blue). Scale bar in C upper panel: 5 μm; applies to top two rows. Scale bars: 5 μm. See also Fig. S1.

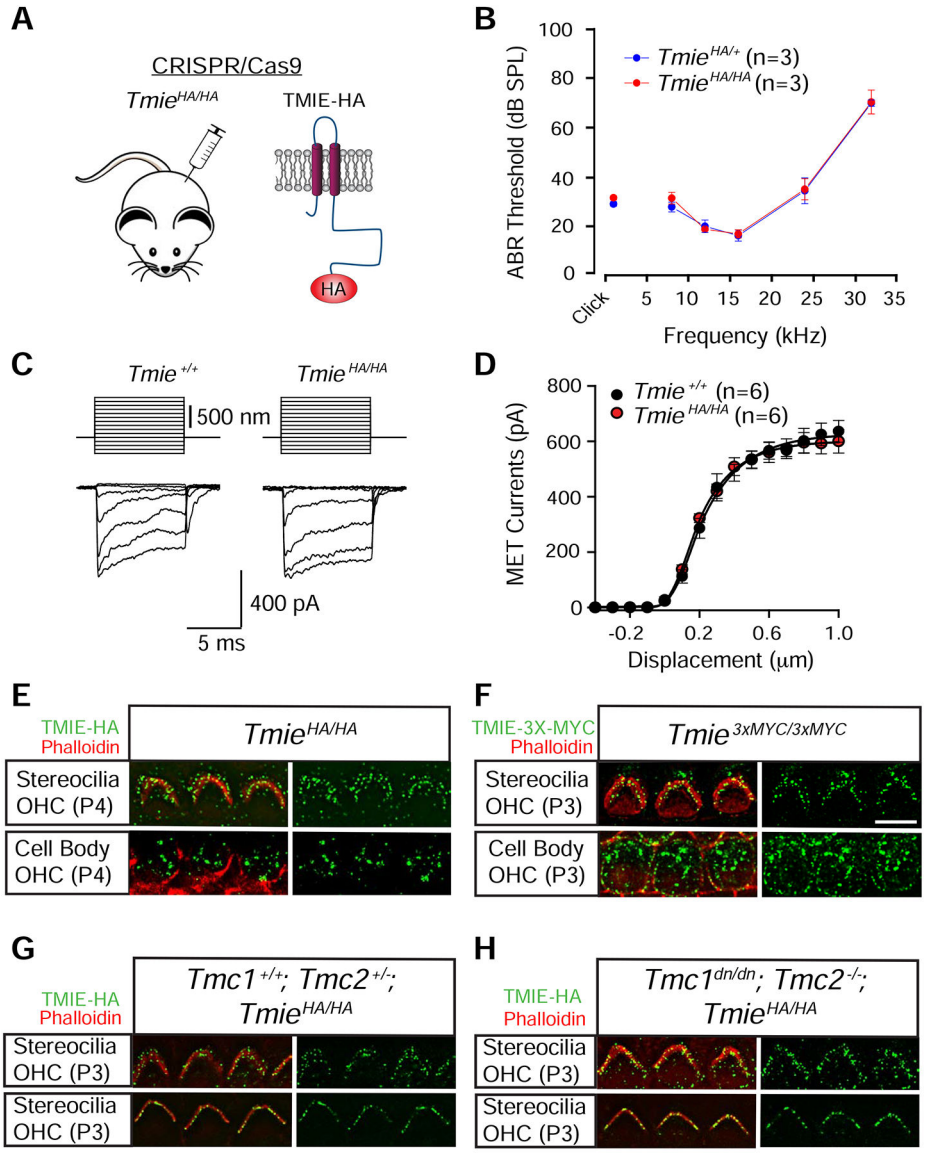

Figure 2. TMC1 and TMC2 do not affect TMIE localization.

(A) Schematic of generation of mouse strains with epitope-tag endogenous TMIE. (B) Auditory brainstem response (ABR) thresholds in response to click and pure tone stimuli for *Tmie*$^{HA/+}$ (n=3) and *Tmie*$^{HA/HA}$ (n=3) mice at ~5 weeks of age. (C) Mechanotransduction currents in OHCs from wild-type and *Tmie*$^{HA/HA}$ mice at P6–7 in response to a set of 10 ms hair bundle deflections ranging from −400 nm to 1000 nm (100 nm steps). (D) Current/displacement plot from similar data as shown in (C) (mean ± SEM). (E) Cochlear whole mounts from P4 *Tmie*$^{HA/HA}$ mice immunostained for HA (green) and phalloidin (red) to label OHCs. (F) Cochlear whole mounts from P3 *Tmie*$^{3XMYC/3XMYC}$ mice immunostained for MYC (green) and phalloidin (red). (G) Cochlear whole mounts from P3 *Tmc1*$^{+/+}$; *Tmc2*$^{+/−}$;*Tmie*$^{HA/HA}$ mice immunostained for HA (green) and phalloidin (red). (H) Cochlear whole mounts from P3 *Tmc1*$^{dn/dn}$;*Tmc2*$^{−/−}$;*Tmie*$^{HA/HA}$ mice immunostained for HA (green) and phalloidin (red). Scale bar in F: 5 μm.

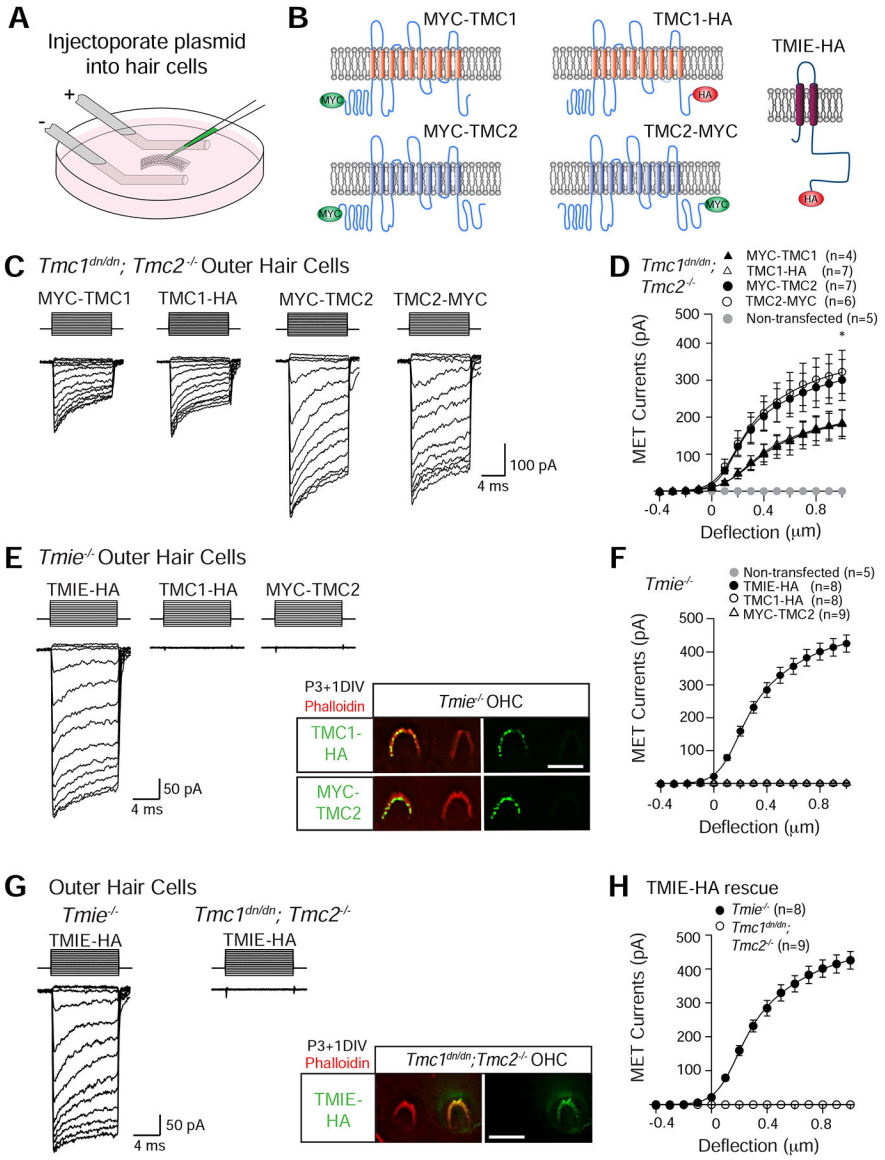

Figure 3. TMIE is essential for TMC1/2 function in hair cells.

(A) Diagram of injectoporation procedure to express genes in hair cells (Xiong et al 2014). (B) Epitope-tagged TMC1/2 and TMIE constructs. (C) Mechanotransduction currents in OHCs from *Tmc1*$^{dn/dn}$*;Tmc2*$^{-/-}$ mice at P3 + 1 day in vitro (DIV) after injectoporation of various constructs. Currents are in response to 10 ms hair bundle deflections from −400 nm to 1000 nm. (D) Current/displacement plot from data as in (C) (mean ± SEM; *, p<0.05 (TMC1 vs TMC2)). (E) Mechanotransduction currents in OHCs from *Tmie*$^{-/-}$ mice at P3 + 1 DIV after injectoporation of various constructs. Currents are in response to 10 ms hair bundle deflections from −400 nm to 1000 nm. Inset shows P3 + 1 DIV injectoporated OHCs immunostained for HA (green, upper row) or MYC (green, lower row) and phalloidin (red). (F) Current/displacement plot from data as in (E) (mean ± SEM). (G) Mechanotransduction currents in OHCs from *Tmie*$^{-/-}$ (left) and *Tmc1*$^{dn/dn}$*;Tmc2*$^{-/-}$ mice (right) at P3 + 1 DIV after injectoporation of TMIE-HA. Inset shows P3 + 1 DIV injectoporated hair cells

immunostained for HA (green) and phalloidin (red). (H) Current/displacement plot from data as in (G) (mean ± SEM). Scale bars: 5 μm. See also Fig. S2.

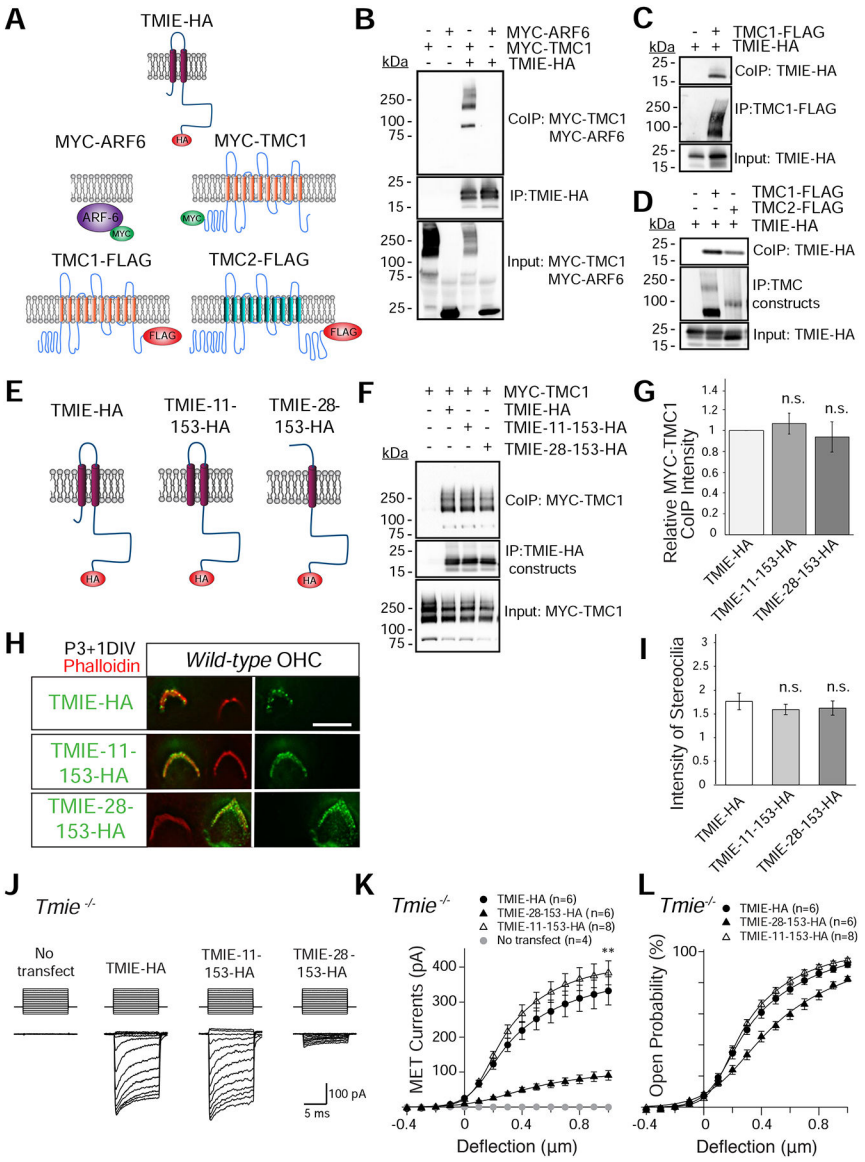

Figure 4. TMIE binds to TMC1 and TMC2 and N-terminal deletions affect TMIE function.

(A, E) Schematic depicting constructs used for CoIP experiments. (B–D) HEK293 cells were transfected with the constructs indicated on top of each panel. Immunoprecipitations (IP) were carried out with HA- (B) or Flag- (C,D) conjugated agarose beads, followed by Western blotting to detect epitope-tagged proteins (upper rows, CoIP; middle rows, IP; lower rows, input). Molecular weights of proteins (in kDa) indicated left of blots. (F) CoIP experiment from HEK293 cells using constructs indicated at top of panel. IP carried out with HA-conjugated agarose beads, followed by Western blotting to detect tagged proteins (upper panels, CoIP; middle row, IP; lower rows, input). (G) Quantification of CoIP results from 4 independent experiments. Binding of TMIE constructs to MYC-TMC1 was normalized to full-length TMIE-HA values (mean ± SEM; n.s., not significant). (H) Examples of OHCs from P3+1 DIV wild-type mice injectoporated with TMIE constructs and immunostained for HA (green) and phalloidin (red). (I) Quantification of stereocilia expression for TMIE

constructs using fluorescent intensities from data as in (H). (mean ± SEM; expressed as a ratio of stereocilia intensity to cell body intensity; n.s., not significant). Number of cells: TMIE-HA, n=13; TMIE-11–153-HA, n=16; TMIE-28–153-HA, n=11. (J) Mechanotransduction currents in OHCs from *Tmie*$^{-/-}$ mice at P3 + 1 DIV after injectoporation with indicated constructs. Currents are in response to a set of 10 ms hair bundle deflections ranging from −400 nm to 1000 nm. (K, L) Current/displacement plots and probability/displacement plots from similar data as in (J) (mean ± SEM; **, $p<0.01$; TMIE-28153-HA vs TMIE-HA).

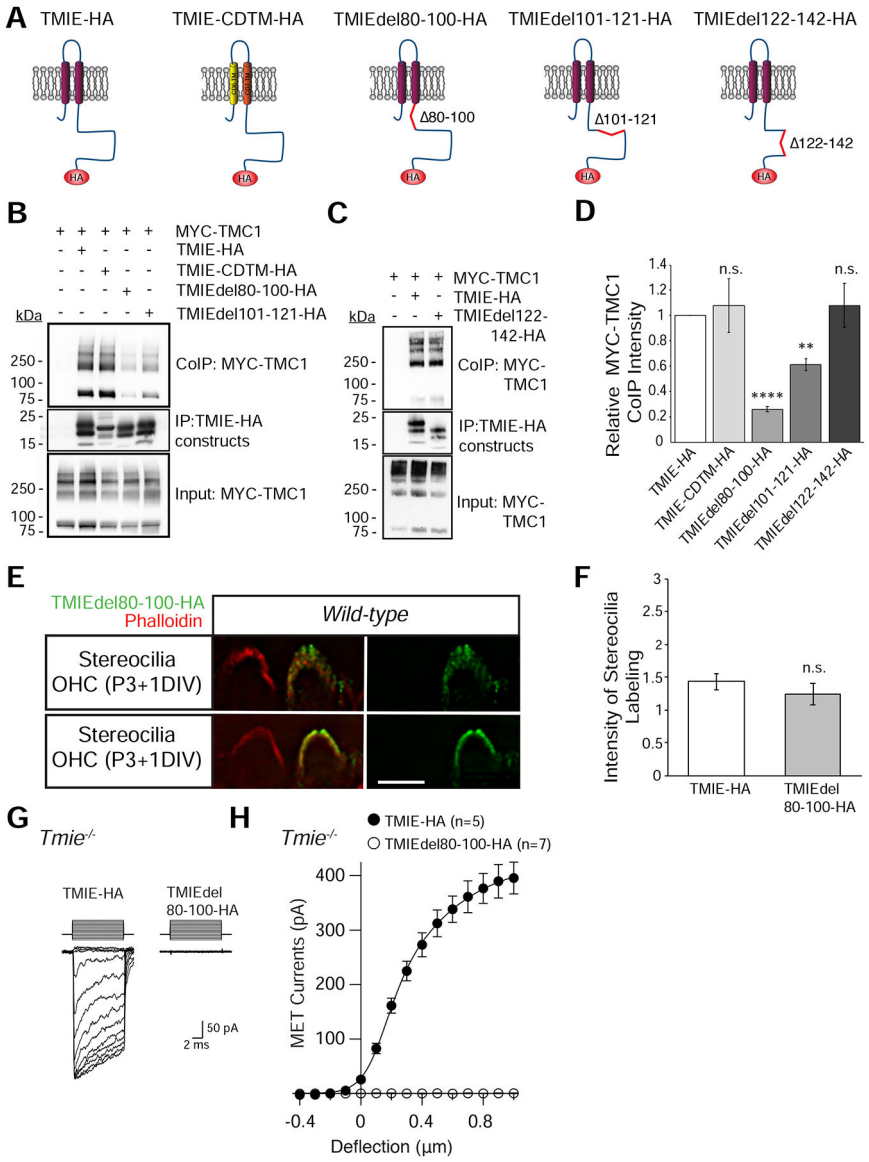

Figure 5. A region in the TMIE C-terminal cytoplasmic domain is required for binding to TMC1 and for mechanotransduction.

(A) Schematic depicting epitope-tagged constructs. (B–C) HEK293 cells were transfected with the constructs indicated on top of each panel. IPs were carried out with HA-conjugated agarose beads, followed by Western blotting to detect tagged proteins (upper panels, CoIP; middle row, IP; lower rows, input). Molecular weights of proteins (in kDa) are indicated. (D) Quantification of CoIP results from a minimum of 3 independent experiments each. Binding of TMIE constructs to MYC-TMC1 normalized to wild-type TMIE-HA values (mean ± SEM; n.s., not significant, **, p<0.01, ****, p<0.0001). (E) Examples of OHCs from P3+1 DIV wild-type mice injectoporated with TMIEdel80–100-HA and immunostained for HA (green) and phalloidin (red). (F) Quantification of stereocilia expression for TMIEdel80–100-HA using fluorescent intensities from data as in (E) (mean ± SEM; expressed as a ratio of stereocilia intensity to cell body intensity). Numbers of cells: TMIE-HA, n=5; TMIEdel80–100-HA, n=4. (G) Mechanotransduction currents in OHCs from *Tmie*$^{-/-}$ mice

at P3 + 1 DIV after injectoporation of indicated constructs. Currents are in response to a set of 10 ms hair bundle deflections ranging from −400 nm to 1000 nm. (H) Current/displacement plot from similar data as in (G) (mean ± SEM). Numbers of cells: TMIE-HA, n=5; TMIEdel80–100-HA, n=7. Scale bar in E: 5 μm.

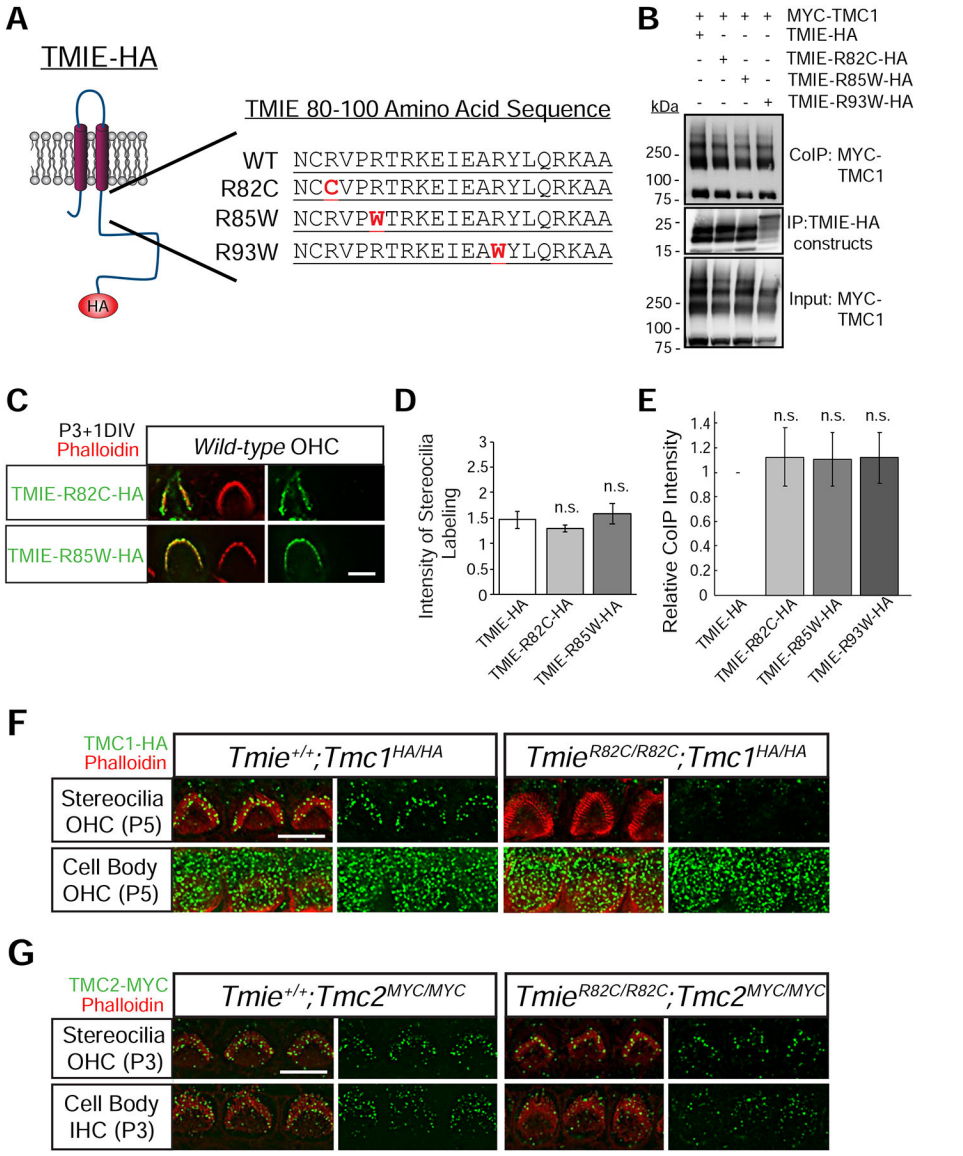

Figure 6. Analysis of deafness-associated point mutations in TMIE.

(A) Schematic depicting constructs containing TMIE point mutations associated with deafness (Naz et al., 2002; Zhao et al., 2014). (B) HEK293 cells were transfected with the constructs indicated on top to perform CoIP experiments. IPs were carried out with HA-conjugated agarose beads, followed by Western blotting to detect tagged proteins (upper panels, CoIP; middle row, IP; lower rows, input). Molecular weights of proteins (in kDa) are indicated. (C) Examples of OHCs from P3+1 DIV wild-type mice injectoporated with TMIE-R82C-HA (top row) and TMIE-R85W-HA (bottom row) and immunostained for HA (green) and phalloidin (red). (D) Quantification of stereocilia expression using fluorescent intensities from data as in (C) (mean ± SEM; expressed as a ratio of stereocilia intensity to cell body intensity). Number of cells: TMIE-HA, n=13; TMIE-R82C-HA, n=7; TMIE-R85W-HA, n=17. (E) Quantification of CoIP results from (B). Quantification from a minimum of 5 independent experiments each. Binding of TMIE constructs to MYC-TMC1

normalized to wild-type TMIE-HA values (mean ± SEM; n.s., not significant) (F) Cochlear whole mounts from P5 $Tmie^{+/+};Tmc1^{HA/HA}$ (left) and $Tmie^{R82C/R82C};Tmc1^{HA/HA}$ mice (right) stained for HA (green) and phalloidin (red) to reveal localization of TMC1 in OHCs. (G) Cochlear whole mounts from P3 $Tmie^{+/+};Tmc2^{Myc/Myc}$ (left) and $Tmie^{R82C/R82C};Tmc2^{Myc/Myc}$ mice (right) stained for MYC (green) and phalloidin (red) to reveal localization of TMC2 in OHCs or IHCs. Scale bars: 5 μm. See also Fig. S3.

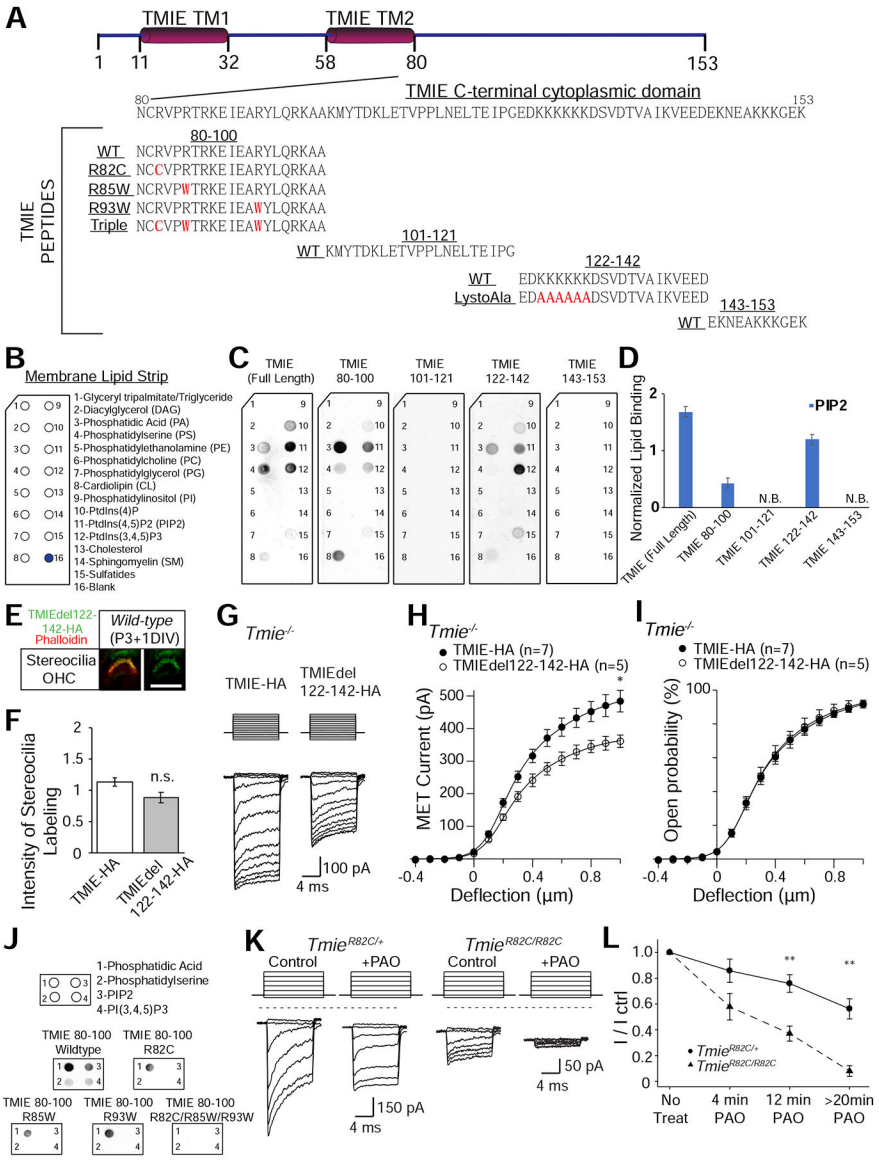

Figure 7. Point mutations in the TMIE cytoplasmic domain affect pore properties of the mechanotransduction channel in OHCs.

(A) Mechanotransduction currents in OHCs from *Tmie*$^{R82C/+}$ and *Tmie*$^{R82C/R82C}$ mice at P5 in response to a set of 10 ms hair bundle deflections ranging from −400 nm to 1000 nm. (B,C) Current/displacement plot and open probability/displacement plot from similar data as in (A) (mean ± SEM). (D) Single channel events elicited by 300 nm stereocilia deflections in OHCs from P3–4 *Tmie*$^{+/+}$ (left) and *Tmie*$^{R82C/R82C}$ (right) mice (C = closed state, O = open state). Ensemble averages of 15 traces at bottom. (E) Amplitude histograms generated from the fourth trace in (D). Gaussian fits of the two peaks in the histograms determine a single-channel current, which is indicated in the panel. (F) Histograms of open-time for single-channel events for *Tmie*$^{+/+}$ (left) and *Tmie*$^{R82C/R82C}$ (right) from data as in (D). Curves are single-exponential fits with time constant Tau of 2.08 ms for *Tmie*$^{+/+}$ (298 events from 12 cells, left) and 1.94 for *Tmie*$^{R82C/R82C}$ (335 events from 13 cells, right). (G) Summary plot of single-channel currents for *Tmie*$^{+/+}$ and *Tmie*$^{R82/R82C}$ cells. Average single-channel

current was reduced from 4.32 ± 0.12 pA (n=72) to 3.40 ± 0.13 pA (n=50) (mean ± SEM; ***, $p<0.001$). (H) Experiments to examine reversal potential and relative Ca^{2+} permeability (P_{Ca}/P_{Cs}). Hair cell membrane was held at various potentials (in 20 mV increments from −89 mV to +111 mV), and the hair bundle was mechanically stimulated to elicit currents at each holding potential. Top, mechanical stimulus paradigm; bottom, mechanotransduction currents in OHCs from *Tmie*$^{R82C/+}$; *Tmc1*$^{dn/dn}$ and *Tmie*$^{R82C/R82C}$; *Tmc1*$^{dn/dn}$ mice at P5. (I). Left: Current/voltage plot averaged at various membrane potentials for data as in (H). Center: Magnified current/voltage plot indicates reversal potential as the traces cross the X-axis. Right: Current/voltage relations were normalized to maximal currents at +111mV to account for differences in current amplitude in controls and mutants. Current/voltage plots were fitted with a single-site binding model. (J) Reversal potential (R_v) plots for OHCs calculated from (H,I) (29.37±1.48 mV vs 23.71 ± 2.03 mV, Mean ± SEM, *, $p<0.05$) (K) Relative Ca^{2+} permeability plots calculated using the Goldman-Hodgkin-Katz equation (6.71 ± 0.70 vs 4.69 ± 0.63, Mean ± SEM, *, $p<0.05$). See also Figs. S4 and S5.

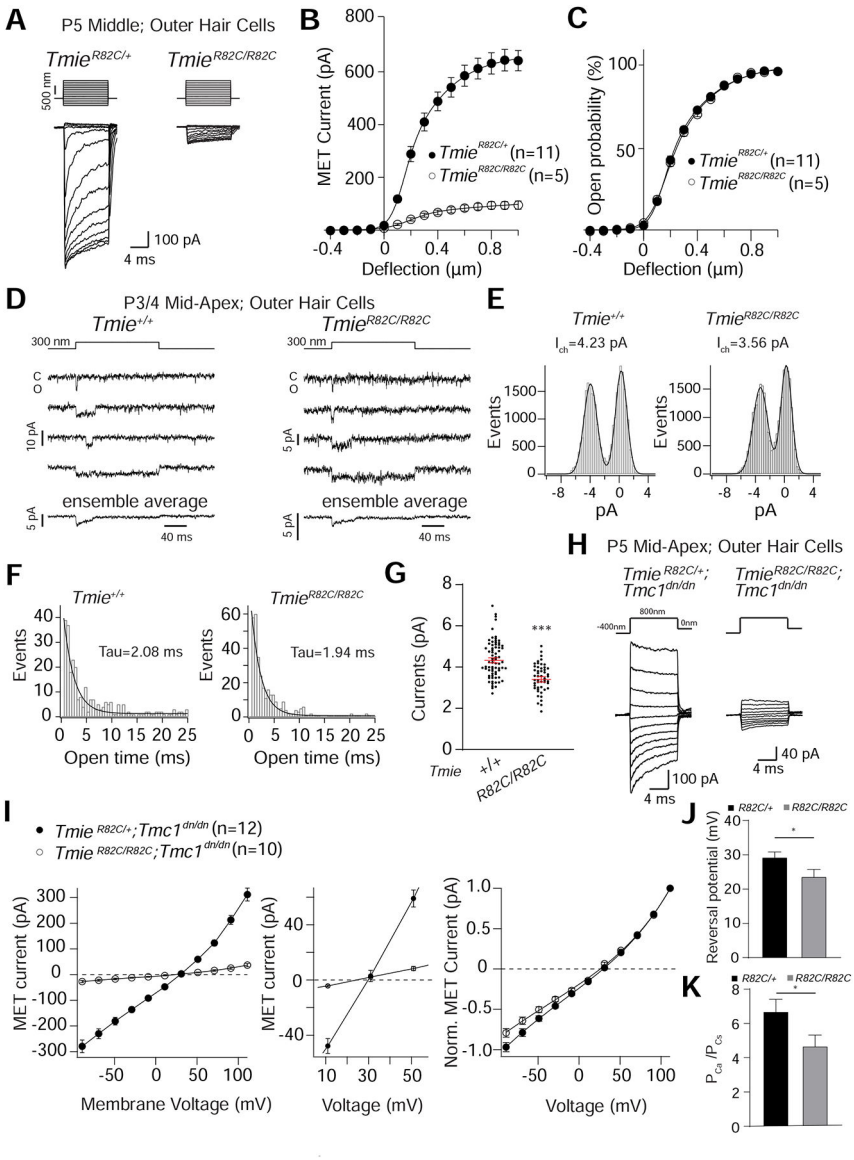

Figure 8. Domains in the C-terminal cytoplasmic domain of TMIE critical for lipid binding and mechanotransduction.

(A) Schematic depicting the TMIE C-terminal cytoplasmic domain, and HA-tagged synthetic peptides used in lipid binding experiments. Mutations in red. (B) Diagram of a Membrane Lipid Strip used in (C, D) and (J). (C) Representative results from Membrane Lipid Strip assays. Membranes were incubated with proteins/peptides listed above membranes, followed by antibody detection using TMIE antibodies (full length TMIE) or HA antibodies (peptides). (D) Quantification of PIP_2 binding intensity, normalized to Phosphatidic Acid binding intensity (mean ± SEM from 3 independent experiments). (E) Examples of OHCs from P3+1 DIV wild-type mice injectoporated with TMIEdel122–142-HA and immunostained for HA (green) and phalloidin (red). (F) Quantification of stereocilia expression for TMIEdel122–142-HA using fluorescent intensities from data as in (E) (mean ± SEM; expressed as a ratio of stereocilia intensity to cell body intensity; n.s., not significant). Number of cells: TMIE-HA, n=4; TMIEdel122–142-HA, n=4. (G)

Mechanotransduction currents in OHCs from *Tmie*$^{-/-}$ mice at P3 + 1 DIV after injectoporation of TMIE constructs. Currents are in response to a set of 10 ms hair bundle deflections ranging from −400 nm to 1000 nm. (H,I) Current/displacement plots and open probability/displacement plots from similar data as in (G) (mean ± SEM; *, $p<0.05$). (J) Representative results from Membrane Lipid Strip assays using wildtype TMIE 80–100 and deafness-associated mutant peptides. Top: legend identifying lipids corresponding to each lipid spot. Lower panels show representative examples of binding results. Peptides listed above images. (K) Mechanotransduction currents in OHCs from *Tmie*$^{R82C/+}$ (left) and *Tmie*$^{R82C/R82C}$ (right) mice at P5 in response to a set of 10 ms hair bundle deflections ranging from −400 nm to 1000 nm. Example traces are for each genotype before (control) and after 12 minute PAO treatment (Effertz et al., 2017). (L) Summary graph showing time-course of changes to mechanotransduction currents during PAO treatment for *Tmie*$^{R82C/+}$ and *Tmie*$^{R82C/R82C}$ from data as in (K) (mean ± SEM; **, $p<0.01$). Scale bar in E: 5 μm. See also Figs. S6 and S7.

KEY RESOURCES TABLE

REAGENT or RESOURCE	SOURCE	IDENTIFIER
Antibodies		
Rabbit anti-HA	Cell Signaling	Cat#: 3724; RRID:AB_1549585
Rabbit anti-MYC	Cell Signaling	Cat#: 2278; RRID:AB_490778
Rabbit anti-PCDH15-CD2	Webb et al 2011	N/A
Rabbit anti-LHFPL5/TMHS	Xiong et al 2012	N/A
Rabbit anti-CDH23	Siemens et al 2004	N/A
Rabbit anti-PMCA2	Abcam	Cat#:ab3529; RRID:AB_303878
Goat anti-Rabbit IgG F(ab')2, Alexa Fluor 488	Invitrogen	Cat#: A-11070; RRID:AB_2534114
Goat anti-Rabbit IgG F(ab')2, Alexa Fluor 555	Invitrogen	Cat#: A-21430; RRID:AB_2535851
EZ-View Red HA Affinity Gel	Sigma	Cat#: E6779; RRID:AB_10109562
EZ-View Red FLAG M2 Affinity Gel	Sigma	Cat#: F2426; RRID:AB_2616449
Mouse anti-FLAG M2	Sigma	Cat#: RRID:AB_262044
Veriblot	Abcam	Cat#: ab131366
Veriblot anti Mouse	Abcam	Cat#: ab131368
Rabbit anti-TMIE	Sigma	Cat# HPA038298, RRID:AB_10675792
Rabbit anti-GST	Cell Signaling	Cat# 2625, RRID:AB_490796
Chemicals, Peptides, and Recombinant Proteins		
Cas9 Protein	PNA Bio	Cat#: CP01–20
Tris-HCl	Sigma	Cat#: T5941
EDTA	Sigma	Cat#: E5134
DMEM+Glutamax medium	Gibco	Cat#: 10569–010
Antibiotic-Antimycotic supplement	Gibco	Cat#: 15240–062
DMEM/F12 medium	Gibco	Cat#: 11330–032
Fetal Bovine Serum, Heat Inactivated	Sigma	Cat#: F4135
Ampicillin	Sigma	Cat#: A9518
Sodium Chloride	VWR	Cat#: 0241
Sodium phosphate monobasic	Sigma	Cat#: S8282
Potassium Chloride	Fisher Scientific	Cat#: P217
Calcium Chloride	Fisher Scientific	Cat#: M13841
Magnesium Chloride	Sigma	Cat#: M8266
Glucose	Sigma	Cat#: G7021
HEPES	Sigma	Cat#: H4034
BAPTA	Sigma	Cat#: A4926
EGTA	VWR	Cat#: 0732
Magnesium-ATP	Sigma	Cat#: A9187
Sodium-GTP	Sigma	Cat#: G8877
Cesium Chloride	Sigma	Cat#: 203025

REAGENT or RESOURCE	SOURCE	IDENTIFIER
D(−)-N-Methylglucamine	Sigma	Cat#:6284408
Phenylarsine oxide (PAO)	Sigma	Cat#: 521000
DMSO	Sigma	Cat#: D2650
Paraformaldehyde	Electron Microscopy Sciences	Cat#: 15714
1X HBSS medium	Gibco	Cat#: 14175095
Normal Goat Serum, Heat Inactivated	Gemini Biosciences	Cat#: 100–109
Triton X-100	Sigma	Cat#: T9284
Alexa Fluor Plus 405 Phalloidin	Life Technologies	Cat#: A30104
Alexa Fluor 488 Phalloidin	Life Technologies	Cat#: A12379
Alexa Fluor 555 Phalloidin	Life Technologies	Cat#: A34055
Prolong Gold	ThermoFisher	Cat#: P10144
Lipofectamine 3000	ThermoFisher	Cat#: L3000015
Tris/Tham	Fisher	Cat#: T370–3
NP-40	Sigma	Cat#: I3021
Sodium Deoxycholate	Sigma	Cat#: 6750
Sodium Dodecyl Sulfate	Sigma	Cat#: 75746
Complete Mini Protease Inhibitor Tablet, EDTA-free	Roche	Cat#: 11836170001
4x Bolt LDS Sample Buffer	Life Technologies	Cat#: B0007
10x Bolt Sample Reducing Agent	Life Technologies	Cat#: B0009
4–12% Bolt Bis-Tris Plus Gels	Life Technologies	Cat#: NW04122BOX
20x Bolt MOPS SDS Running Buffer	Life Technologies	Cat#: B0001
20x Bolt Transfer Buffer	Life Technologies	Cat#: BT00061
Methanol	VWR	Cat#: BDH1135–4LP
ECL Prime Blocking Reagent	GE	Cat#: RPN418
Tween-20	Sigma	Cat#: P7949
Clarity Western ECL Substrate	Bio-Rad	Cat#: 1705060
Membrane Lipid Strips	Echelon Biosciences	Cat#: P-6002
PIP Strips	Echelon Biosciences	Cat#: P-6001
Bovine Serum Albumin, fatty acid free	Sigma	Cat#: A8806
Recombinant Human TMIE protein	Origene	Cat#: TP320050
HA-Tagged Synthetic TMIE peptide fragments	This paper	N/A
Experimental Models: Cell Lines		
Human: HEK-293	ATCC	Cat# CRL-1573
Experimental Models: Organisms/Strains		
Tmie$^{-/-}$ (*Tmie*^{LacZ}) mice	Zhao et al 2014	MGI#:5784557
Tmc1dn (Tmc1 deafness) mice	Kurima et al 2002	MGI#:1856845
Tmc2$^{-/-}$ mice	Kim et al 2013	MGI#:5007364
Tmc1-HA mice	This paper	N/A
Tmc2-MYC mice	This paper	N/A

REAGENT or RESOURCE	SOURCE	IDENTIFIER
Tmie-HA mice	This paper	N/A
Tmie-3X-MYC mice	This paper	N/A
Tmie-R82C mice	This paper	N/A
Tmie-R85W mice	This paper	N/A
C57BL/6J mice	Jackson Laboratories	Cat#: 000664; RRID:IMSR JAX:000664
ICR mice	Envigo	Cat#: Hsd:ICR (CD-1)
Oligonucleotides		
Target-specific crRNAs	This paper/IDT	N/A
tracrRNA	Dharmacon	Cat#: U-002005–05
Target-specific ssDNA	This paper/IDT Ultramer DNA Oligos	N/A
Recombinant DNA		
pN3	Zhao et al 2014	N/A
pN3-TMIE-HA	Zhao et al 2014	N/A
pN3-TMIE-11–153-HA	This paper	N/A
pN3-TMIE-28–153-HA	This paper	N/A
pN3-TMIE-CDTM-HA	This paper	N/A
pN3-TMIEdel80–100-HA	This paper	N/A
pN3-TMIEdel101–121-HA	This paper	N/A
pN3-TMIEdel122–142-HA	This paper	N/A
pN3-TMIE-R82C-HA	Zhao et al 2014	N/A
pN3-TMIE-R85W-HA	Zhao et al 2014	N/A
pN3-TMIE-R93W-HA	Zhao et al 2014	N/A
pCAGEN	Matsuda et al 2004	Cat#: Addgene #11160; RRID:Addgene_11160
pCAGEN-MYC-TMC1	This paper	N/A
pCAGEN-TMC1-HA	This paper	N/A
pCAGEN-MYC-TMC2	This paper	N/A
pCAGEN-TMC2-MYC	This paper	N/A
pCAGEN-TMC1-FLAG	This paper	N/A
pCAGEN-TMC2-FLAG	This paper	N/A
pCAGEN-MYC-ARF6	This paper	N/A
Software and Algorithms		
Deltavision Elite Software (SoftWoRx Resolve 3D)	GE	https://www.gelifesciences.com/en/ee/shop/deltavision-elite-high-resolution-microscope-p-04420
Igor pro 7	WaveMetrics	https://www.wavemetrics.com/
Imaris 8.3.1	Oxford Instruments	http://www.bitplane.com/imaris
TDT System 3	Tucker-Davis Technology	https://www.tdt.com/products/
Origin Pro 7.5	Origin Lab	https://www.originlab.com/
Graph-Pad Prism 5	Graph Pad Software	https://www.graphpad.com/scientific-software/prism/

REAGENT or RESOURCE	SOURCE	IDENTIFIER
ImageJ	Schneider et al., 2012	https://imagej.nih.gov/ij/index.html
Patchmaster 2.35	HEKA	http://www.heka.com/downloads/downloads_main.html
Micro-Manager 1.4 software.	Edelstein et al., 2010	https://micro-manager.org/wiki/
Adobe Illustrator 2020	Adobe	https://www.adobe.com/